

PICO: Probe of Inflation and Cosmic Origins

Thematic Area: Space Based Projects

Lead Author: Shaul Hanany (hanany@umn.edu)¹

Authors

Marcelo Alvarez ^{9,16}	Brendan P. Crill ⁶	Eric Hivon ³⁰	Levon Pogosian ⁴⁷
Emmanuel Artis ¹²	Gianfranco De Zotti ³⁵	Renée Hložek ⁴⁰	Clem Pryke ¹
Peter Ashton ^{24,16,9}	Jacques Delabrouille ^{5,12}	Johannes Hubmayr ¹⁹	Giuseppe Puglisi ^{48,49}
Jonathan Aumont ²⁵	Eleonora Di Valentino ³⁶	Bradley R. Johnson ⁴¹	Mathieu Remazeilles ³³
Ragnhild Aurién ²⁶	Joy Didier ³⁷	William Jones ⁴	Graca Rocha ^{6,8}
Ranajoy Banerji ²⁶	Olivier Doré ^{6,8}	Terry Jones ¹	Marcel Schmittfull ¹⁸
R. Belen Barreiro ²⁷	Hans K. Eriksen ²⁶	Lloyd Knox ²⁰	Douglas Scott ⁵⁰
James G. Bartlett ^{5,6}	Josquin Errard ⁵	Al Kogut ²¹	Peter Shirron ²¹
Soumen Basak ²⁸	Tom Essinger-Hileman ²¹	Marcos López-Caniego ⁴²	Ian Stephens ⁵¹
Nick Battaglia ⁷	Stephen Feeney ¹⁷	Charles Lawrence ⁶	Brian Sutin ⁶
Jamie Bock ^{8,6}	Jeffrey Filippini ³⁸	Alex Lazarian ⁴³	Maurizio Tomasi ⁵²
Kimberly K. Boddy ²	Laura Fissel ¹⁴	Zack Li ⁴	Amy Trangsrud ⁶
Matteo Bonato ²⁹	Raphael Flauger ¹⁵	Mathew Madhavacheril ⁴	Alexander van Engelen ²³
Julian Borrill ^{9,10}	Unni Fuskeland ²⁶	Jean-Baptiste Melin ¹²	Flavien Vansyngel ⁵³
François Bouchet ³⁰	Vera Gluscevic ³⁹	Joel Meyers ⁴⁴	Ingunn K. Wehus ²⁶
François Boulanger ³¹	Krzysztof M. Gorski ⁶	Calum Murray ⁵	Qi Wen ¹
Blakesley Burkhardt ³²	Dan Green ¹⁶	Mattia Negrello ⁴⁵	Siyao Xu ⁴³
Jens Chluba ³³	Shaul Hanany ¹	Giles Novak ⁴⁶	Karl Young ¹
David Chuss ¹¹	Brandon Hensley ⁴	Roger O'Brient ^{6,8}	Andrea Zonca ⁵⁴
Susan E. Clark ^{18,34}	Diego Herranz ²⁷	Christopher Paine ⁶	
Joelle Cooperrider ⁶	J. Colin Hill ^{17,18}	Tim Pearson ⁸	

Endorsers

Maximilian Abitbol	Carlo Burigana	Kyle Helson	Tomotake Matsumura
Zeeshan Ahmed	Giovanni Cabass	Sophie Henrot-Versillé	Darragh McCarthy
David Alonso	Robert Caldwell	Thiem Hoang	P. Daniel Meerburg
Mustafa A. Amin	John Carlstrom	Kevin M. Huffenberger	Alessandro Melchiorri
Adam Anderson	Xingang Chen	Kent Irwin	Marius Millea
James Annis	Francis-Yan Cyr-Racine	Reijo Keskitalo	Amber Miller
Jason Austermann	Paolo de Bernardis	Rishi Khatri	Joseph Mohr
Carlo Baccigalupi	Tijmen de Haan	Chang-Goo Kim	Lorenzo Moncelsi
Darcy Barron	C. Darren Dowell	Theodore Kisner	Pavel Motloch
Ritoban Basu Thakur	Cora Dvorkin	Arthur Kosowsky	Tony Mroczkowski
Elia Battistelli	Chang Feng	Ely Kovetz	Suvodip Mukherjee
Daniel Baumann	Ivan Soares Ferreira	Kerstin Kunze	Johanna Nagy
Karim Benabed	Aurelien Fraisse	Guilaine Lagache	Pavel Naselsky
Bradford Benson	Andrei V. Frolov	Daniel Lenz	Federico Nati
Paolo de Bernardis	Nicholas Galitzki	François Levrier	Paolo Natoli
Marco Bersanelli	Silvia Galli	Marilena Loverde	Michael Niemack
Federico Bianchini	Ken Ganga	Philip Lubin	Elena Orlando
Daniel Bilbao-Ahedo	Tuhin Ghosh	Juan Macias-Perez	Bruce Partridge
Colin Bischoff	Sunil Golwala	Nazzareno Mandolesi	Marco Peloso
Sebastian Bocquet	Riccardo Gualtieri	Enrique Martínez-	Francesco Piacentini
J. Richard Bond	Jon E. Gudmundsson	González	Michel Piat
Jeff Booth	Nikhel Gupta	Carlos Martins	Elena Pierpaoli
Sean Bryan	Nils Halverson	Silvia Masi	Giampaolo Pisano

Nicolas Ponthieu	Benjamin Saliwanchik	Eric Switzer	Jan Vrtilek
Giuseppe Puglisi	Neelima Sehgal	Andrea Tartari	Benjamin Wallisch
Benjamin Racine	Sarah Shandera	Grant Teply	Benjamin Wandelt
Christian Reichardt	Erik Shirokoff	Peter Timbie	Gensheng Wang
Christophe Ringeval	Anže Slosar	Matthieu Tristram	Scott Watson
Karwan Rostem	Tarun Souradeep	Caterina Umiltà	Edward J. Wollack
Anirban Roy	Suzanne Staggs	Rien van de Weygaert	Zhilei Xu
Jose Alberto Rubino-Martin	George Stein	Vincent Vennin	Siavash Yasini
Matarrese Sabino	Radek Stompor	Licia Verde	
Maria Salatino	Rashid Sunyaev	Patricio Vielva	
	Aritoki Suzuki	Abigail Vieregg	

Affiliations

1. University of Minnesota - Twin Cities.
2. Johns Hopkins University.
3. Carnegie Mellon University.
4. Princeton University.
5. APC, Univ Paris Diderot, CNRS/IN2P3, CEA/Irfu, Obs de Paris, Sorbonne Paris Cité, France.
6. Jet Propulsion Laboratory, California Institute of Technology.
7. Cornell University.
8. California Institute of Technology.
9. Lawrence Berkeley National Laboratory.
10. Space Sciences Laboratory, University of California, Berkeley.
11. Villanova University.
12. IRFU, CEA, Université Paris-Saclay, France.
13. University of Pennsylvania.
14. National Radio Astronomy Observatory.
15. University of California, San Diego.
16. University of California, Berkeley.
17. Center for Computational Astrophysics, Flatiron Institute.
18. Institute for Advanced Study, Princeton.
19. National Institute of Standards and Technology.
20. University of California, Davis.
21. NASA Goddard Space Flight Center.
22. University of Michigan.
23. Canadian Institute for Theoretical Astrophysics, University of Toronto, Canada.
24. Kavli Institute for the Physics and Mathematics of the Universe (WPI).
25. IRAP, Université de Toulouse, France.
26. University of Oslo, Norway.
27. Instituto de Física de Cantabria (CSIC-Universidad de Cantabria), Spain.
28. School of Physics, Indian Institute of Science Education and Research Thiruvananthapuram, India.
29. INAF-Istituto di Radioastronomia and Italian ALMA Regional Centre, Italy.
30. Institut d'Astrophysique de Paris, CNRS and Sorbonne Université, France.
31. Ecole Normale Supérieure, Paris, France.
32. Rutgers University.
33. JBCA, University of Manchester.
34. Hubble Fellow
35. INAF-Osservatorio Astronomico di Padova, Italy.
36. University of Manchester.
37. University of Southern California.
38. University of Illinois, Urbana-Champaign.
39. University of Florida.
40. Department of Astronomy & Astrophysics and Dunlap Institute, University of Toronto, Canada.
41. Columbia University.
42. European Space Astronomy Centre.
43. University of Wisconsin - Madison.
44. Southern Methodist University.
45. Cardiff University School of Physics and Astronomy.
46. Northwestern University.
47. Simon Fraser University.
48. Stanford University.
49. Kavli Institute for Particle Astrophysics and Cosmology.
50. University of British Columbia, Canada.
51. Harvard-Smithsonian Center for Astrophysics.
52. Università degli studi di Milano.
53. Institut d'Astrophysique Spatiale, CNRS, Univ. Paris-Sud, Université Paris-Saclay, France.
54. San Diego Supercomputer Center, University of California, San Diego.

This research was funded by a NASA grant NNX17AK52G to the University of Minnesota / Twin Cities, by the Jet Propulsion Laboratory, California Institute of Technology, under a contract with the National Aeronautics and Space Administration, and by Lockheed Martin Corporation.

Substantial contributions to the development of PICO were volunteered by scientists at many institutions world-wide. They are very gratefully acknowledged.

The information presented about the PICO mission concept is pre-decisional and is provided for planning and discussion purposes only.

The cost information contained in this document is of a budgetary and planning nature and is intended for informational purposes only. It does not constitute a commitment on the part of JPL and/or Caltech.

1 Executive Summary

The Probe of Inflation and Cosmic Origins (PICO) is an imaging polarimeter that will scan the sky for 5 years in 21 frequency bands spread between 21 and 799 GHz. It will produce full-sky surveys of intensity and polarization with a final combined-map noise level equivalent to 3300 *Planck* missions for the baseline required specifications, and according to our current best-estimate would perform as 6400 *Planck* missions. With these capabilities, unmatched by any other existing or proposed platform:

- PICO could determine the energy scale of inflation and give a first, direct probe of quantum gravity by searching for the signal that arises from gravitational waves sourced by inflation and parameterized by the tensor-to-scalar ratio r . The PICO requirement is to reach $r = 5 \times 10^{-4}$ (5σ), a level that is 100 times lower than current upper limits, and 5 times lower than limits forecast by any planned experiment. If the signal is not detected, PICO is the only instrument that can exclude at 5σ (?) models for which the characteristic scale in the potential is the Planck scale, a key threshold in inflation physics.
- The mission will measure the minimum expected sum of the neutrino masses with 4σ confidence, rising to 7σ if the sum is near 0.1 eV. PICO will give two additional independent and equally competitive constraints on the sum of neutrino masses.
- The measurements will either detect or strongly constrain deviations from the standard model of particle physics by counting the number of light particle species N_{eff} in the early universe with $\Delta N_{\text{eff}} < 0.06$ (2σ).
- PICO will elucidate the processes affecting the evolution of cosmic structures by measuring the optical depth to reionization τ with an error $\sigma(\tau) = 0.002$, limited only by the small number of spatial modes available in the largest angular scale CMB polarization.
- The data will give a full sky map of the projected gravitational potential due to all structures in the Universe with the highest signal-to-noise ratio (SNR) relative to any foreseeable experiment, and it will give a catalog of 150,000 clusters extending to their earliest formation redshift. Each of these datasets will be used in combination with other data to constrain the evolution of the amplitude of linear fluctuations $\sigma_8(z)$ with sub-percent accuracy and thus constrain dark energy and modified gravity models.
- PICO will determine the cosmological paradigm of the 2030s by reducing the allowed volume of uncertainty in a 12-dimensional Λ CDM parameter space by a factor of nearly a billion relative to current *Planck* constraints on only six parameters. Such exquisite scrutiny will either give strong validation of the model or require yet-to-be discovered revisions.
- PICO’s maps of the Milky Way, which will have 3000 times more independent pixels compared to those available from *Planck*, will be used to resolve long-standing questions about our own Galaxy including the composition, temperature, and emissivities of Galactic dust, and the relative roles of gas turbulence and magnetic fields in the dynamics of the Galaxy and in the observed low star-formation efficiency.
- The data will constrain generic models of dark matter; enable a search for primordial magnetic fields with sufficient sensitivity to rule them out as the sole source for the largest observed galactic magnetic fields; constrain string theory motivated axions by improving by a factor of 300 constraints on polarization rotation arising from early Universe fields; and will give precise tracing of the evolution with z of thermal pressure in the universe through correlations of the thermal Sunyaev–Zeldovich effect with LSST’s gold sample of galaxies, which will exceed a signal-to-

noise ratio of 1000.

- PICO will give deep, full-sky legacy maps with which astrophysicists across many sub-disciplines will constrain the early phases of galaxy evolution; investigate the early phases of cluster evolution; perform a census of cold dust in thousands of low z galaxies; make cosmic infrared background maps of the anisotropies due to dusty star-forming galaxies; and map magnetic fields in 70 nearby galaxies.

With its broad frequency coverage, PICO is better equipped than any other current or planned instrument to separate the detected signals into their original sources of emission. This capability is important for many of the science goals, and is critical for unveiling the faintest of signals, the telltale signature of inflation, which is already known to be dominated by Galactic foregrounds. PICO’s large multiplicity of independent maps and sky surveys, and its stable thermal environment will give control of systematic uncertainties unmatched by any other platform. Mission operations are simple: PICO has a single instrument that surveys the sky with a continuously repetitive pattern. The required technologies have either already been proven by past missions, or are simple extensions of technologies now being used by sub-orbital experiments.

The science PICO will deliver addresses some of the most fundamental quests of human knowledge. Its science advances will enrich many areas of astrophysics, and will form the basis for the cosmological paradigm of the 2030s and beyond. Many of these advances can only be achieved by a space-based mission. Progress in CMB science requires a scale-up of investment. PICO is the most cost-effective way to achieve this scale-up. It has no competitor in terms of raw sensitivity, and it is the only single-platform instrument with the combination of angular resolution, frequency bands, and control of systematic effects that can deliver the compelling, timely, and broad science.

2 Key Science Goals and Objectives

2.1 Gravitational Waves and Inflation

Measurements of the cosmic microwave background (CMB) BB angular power spectrum are the only foreseeable way to detect inflationary gravitational waves. The strength of the signal, quantified by the tensor-to-scalar ratio r , is a direct measure of the expansion rate of the Universe during inflation, and together with the Friedmann equation, it reveals the energy scale of inflation. A detection of r “would be a watershed discovery”, a quote from the 2010 decadal panel report [1].

PICO will detect primordial gravitational waves if inflation occurred at an energy scale of at least 5×10^{15} GeV, or equivalently $r = 5 \times 10^{-4}$ (5σ). In a community white paper setting targets for measurements of inflationary gravitational waves in the next decade, Shandera et al. [2] quote two theoretically motivated targets: (1) rejecting $r = 0.01$, and (2) rejecting $r = 0.001$. The second threshold is motivated by the goal of rejecting all inflationary models that naturally explain the observed value of the spectral index of primordial fluctuations n_s and having a characteristic scale in the potential that is larger than the Planck scale. They write “If these thresholds are passed without a detection, most textbook models of inflation will be ruled out; and, while the possibility

Table 1.1: Mission Parameters

Full sky CMB polarization map depth ^a :	
Baseline	$0.87 \mu\text{K}_{\text{CMB}}$ arcmin equivalent to 3300 <i>Planck</i> missions
CBE ^b	$0.61 \mu\text{K}_{\text{CMB}}$ arcmin equivalent to 6400 <i>Planck</i> missions
Survey duration / start .	5 yrs / 2029
Orbit type	Sun-Earth L2
Launch mass	2147 kg
Total power	1320 W
Data rate	6.1 Tbits/day
Cost	\$ 958M

^a rms noise in 1×1 arcmin 2 pixel.

^b CBE = Current best estimate.

of an early inflationary phase would still remain viable, the data would then force a significant change in our understanding of the primordial Universe." PICO is the only next decade experiment with the raw sensitivity to reject both targets at high confidence; see Figure 2.1. It is the only next decade experiment that can detect inflationary models that have $r \geq 5 \times 10^{-4}$ at high confidence.

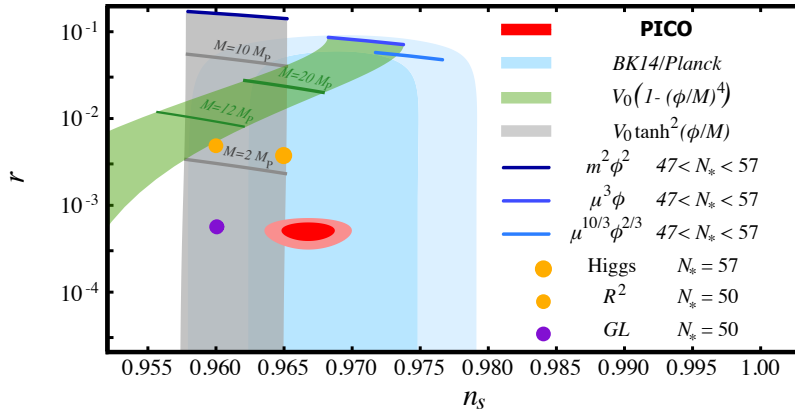


Figure 2.1: Current 1σ and 2σ limits on r and n_s (cyan) and forecasted constraints for a fiducial model with $r = 0.0005$ for PICO, together with predictions for selected models of inflation. Characteristic super-Planckian scales in the potentials are marked with darker lines. GL is the Goncharenko-Linde model (see text).

Uncertainty in the characterization of Galactic foregrounds already limits our ability to constrain r . These foregrounds are anticipated to be nearly 1000 times stronger than next-decade-targeted inflationary B -mode signals at low ℓ multipoles. ‘Lensing’ B -modes, created by gravitational lensing of E -modes, are an additional effective foreground for the higher multipoles. With sufficiently high resolution to remove at least 73% of the lensing effects, and 21 frequency bands to account for foregrounds, no other next-decade experiment is better equipped than PICO to overcome the challenges in robustly finding the faint inflationary signal, or in rejection confusion due to foregrounds.

2.2 Fundamental Particles and Fields

- **Light Relics** The ‘effective number of light relic particle species’ N_{eff} gives information about particle species that are predicted to have existed in the early Universe in extensions of the Standard Model. The canonical value with three neutrino families is $N_{\text{eff}} = 3.046$. Additional light particles contribute a change ΔN_{eff} that is a function only of the decoupling temperature of the additional species and the spin of the particle g . PICO will provide a constraint $\Delta N_{\text{eff}} < 0.06$ (95%) and will either detect new particle species, or constrain the lowest temperature T_F at which any vector particle (spin 1) could have fallen out of equilibrium to a factor of 400 higher than today’s constraint. No other next decade experiment will provide a tighter constraint. [add Neff white paper, and check the statement.](#)

- **Neutrino Mass** The origin, structure, and values of the neutrino masses are among the great outstanding questions about the nature of the Standard Model particles. All cosmological measurements of $\sum m_\nu$ relate the amplitudes of the matter power spectrum and the primordial fluctuation power spectrum A_s . Both are limited by degeneracies; the former is limited by our knowledge of ω_m and the latter by the optical depth to reionization τ . PICO is the only instrument that will self consistently provide three of these four ingredients: τ , A_s from the primary CMB, and the matter power spectrum via CMB lensing. In combination with ω_m coming from DESI and EUCLID data, PICO will give $\sigma(\sum m_\nu) = 14$ meV, giving a 4σ detection of the minimum sum of 58 meV. PICO will measure $\sum m_\nu$ in two additional ways, which will give equivalent constraints.

- **Dark Matter** Cosmological measurements have already confirmed the existence of one relic

that lies beyond the Standard Model: dark matter. CMB experiments are effective in constraining dark matter candidates in the lower mass range, which is not available for terrestrial direct detection experiments [3–8].

PICO’s constraining power comes from making high SNR maps of the lensing-induced deflections of polarized photons, and cosmic-variance limited determinations of the TT , TE and EE spectra up to $\ell \simeq 2500$. For a spin-independent velocity-independent contact-interaction between dark matter and protons, chosen as our fiducial model, PICO will improve upon *Planck*’s dark matter cross-section constraints by a factor of 25 over a broad range of candidate dark matter masses that are largely unavailable for traditional direct detection experiments. If 2% of the total dark content is made of axions, PICO’s measurement of the TT , TE and EE spectra with additional constraints from the lensing reconstruction will detect this species at between 7 and 13σ , depending on the mass range. This is an average improvement of a factor of 10 relative to *Planck*.

- **Primordial Magnetic Fields** One of the long-standing puzzles in astrophysics is the origin of observed 1–10 μG galactic magnetic fields [9]. Producing such fields through a dynamo mechanism requires a primordial seed field [10]. Moreover, μG -strength fields have been observed in proto-galaxies that are too young to have gone through the number of revolutions necessary for the dynamo to work [11]. A 0.1 nG primordial magnetic field (PMF), present at the time of galaxy formation, could provide the seed or even eliminate the need for the dynamo altogether [12]. A detection of PMFs with the CMB would be a major discovery because it would signal new physics beyond the Standard Model, and discriminate among different theories of the early Universe [17–19]. PICO will probe PMFs as weak as 0.1 nG (1σ), a precision not attainable by any next decade experiment, and can thus conclusively rule out the purely primordial (i.e., no-dynamo driven) origin of the largest galactic magnetic fields.

- **Cosmic Birefringence** A number of well-motivated extensions of the Standard Model involve fields with parity-violating coupling [23–25, 25–28]. Their presence may cause cosmic birefringence – a rotation of the polarization of an electromagnetic wave as it propagates across cosmological distances [25, 29, 30]. PICO’s constraints on cosmic birefringence are more stringent than any other next decade experiment [?].

2.3 Cosmic Structure Formation and Evolution

- **The Formation of the First Luminous Sources** A few hundred million years after the Big Bang, the neutral hydrogen gas permeating the Universe was reionized by photons emitted by the first luminous sources to have formed. The nature of these sources and the exact history of this epoch are key missing links in our understanding of structure formation. The reionization of the Universe imprints multiple signals in the CMB, the most important of which is an enhancement in the EE power spectrum at large angular scales $\ell \lesssim 10$ (Fig. ??). This signal gives a direct measurement of the optical depth to the reionization epoch τ and thus to the mean redshift of reionization z_{re} , with very little degeneracy with other cosmological parameters (Fig. ??). The current uncertainty on τ , $\sigma(\tau) = 0.007(1\sigma)$ leaves many unanswered questions including: were the ionizing sources primarily star-forming galaxies or more exotic sources such as supermassive black holes or annihilating dark matter? What was the mean free path of ionizing photons during this epoch? What was the efficiency with which such photons were produced by ionizing sources? Did the reionization epoch extend to $z \sim 15$ –20, as has been claimed recently [36]? With full sky coverage, multiple frequency bands, and ample sensitivity to remove foregrounds, PICO is uniquely suited to make the low- ℓ EE -spectrum measurements and reach cosmic-variance-limited

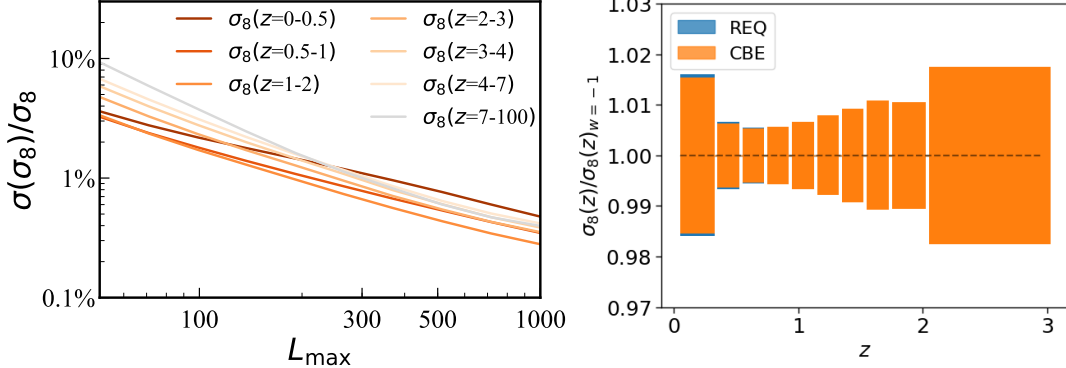


Figure 2.2: Sub-percent constraints on the evolution of σ_8 as a function of redshift will come from two independent PICO products: correlations between PICO’s deep gravitational lensing map (Fig. ??) and LSST’s gold sample of galaxies (left) and cluster counts (right). Fractional uncertainties in σ_8 relative to fiducial Λ CDM values are given as a function of the finest angular scale L_{\max} of the correlation analysis for seven redshift bins (left). The baseline and CBE configurations give essentially the same fractional errors of $\sigma_8(z)$ using cluster counts (right). For LSST we assume: 10 years, 50% sky fraction, 55 galaxies per arcmin² at redshift $z < 3$ with magnitude limit $i < 25.3$ [37], and dropout galaxies at $z > 3$ [38] extrapolating recent Hyper Suprime-Cam observations [39–41], with linear bias $b(z) = 1 + z$.

precision with $\sigma(\tau) = 0.002$, settling some of these questions and significantly constraining the others. Data from PICO’s frequency bands above 400 GHz – which have better than 2 arcmin resolution – will be used to provide clean maps for higher resolution ground-based instruments that can reconstruct the patchy τ field. No other experiment can provide these data **this needs to be improved**.

• Probing the Evolution of Structures via Gravitational Lensing and Cluster Counts The amplitude of linear fluctuations as a function of redshift, parameterized by $\sigma_8(z)$, is a sensitive probe of physical processes affecting growth of structures in the Universe. CMB photons are affected by, and thus probe, $\sigma_8(z)$ as they traverse the entire Universe. The PICO sub-percent constraints on $\sigma_8(z)$, obtained through measurements of gravitational lensing and – independently – using cluster counts, will translate to constraints on dark energy, models of modified gravity, baryonic feedback process, and limits on the particle content of the Universe.

– Gravitational Lensing Matter between us and the last-scattering surface deflects the path of photons through gravitational lensing, imprinting the three-dimensional matter distribution across the volume of the Universe onto the CMB maps. The specific quantity being mapped by the data is the projected gravitational potential ϕ that is lensing the photons. PICO’s data will give a map of ϕ with $\text{SNR} \gg 1$ for each mode in the range $2 \leq L \lesssim 1000$. The SNR on the angular power spectrum $C_L^{\phi\phi}$ will be 560 and 644 for the baseline and CBE configurations, respectively; both values already account for foreground separation, and for $L \lesssim 1000$ they are the highest of any experiment in the next decade, including the higher resolution CMB-S4.

PICO’s ϕ map is a key ingredient in the delensing process that improves constraints on r (§ 2.1) and in extracting neutrino mass constraints (§ 2.2). It will also be used to constrain the properties of quasars and other high-redshift astrophysical tracers of structure. Cross-correlations between the PICO lensing-potential map and wide-field samples of galaxies and quasars – such as from LSST – provide a powerful technique to measure the time dependence of the amplitude of matter fluctuations $\sigma_8(z)$ in tomographic redshift bins. Sub-percent accuracy is obtainable with PICO’s resolution, which will give information extending to $L = 1000$; see the left panel of Fig. 2.2.

– Cluster Counts The distribution of galaxy clusters over redshift is one consequence of the

evolution of structures and is thus a sensitive measure of $\sigma_8(z)$. We forecast that PICO will find $\sim 150,000$ galaxy clusters, assuming the cosmological parameters from *Planck* and using the 70% of sky not obscured by the Milky Way. Information provided by the high frequency bands will mitigate the potential reduction in detection efficiency due to dust emission by cluster members [42]. This catalog will provide σ_8 with sub-percent precision for $0.5 < z < 2$ (Fig. 2.2, right), and a neutrino mass constraint $\sigma(\sum m_\nu) = 14$ meV that is independent from the one coming from the CMB lensing measurements (SO3, § 2.2). A significant fraction of the PICO-detected clusters will also be detected by eROSITA, giving an exceptional catalog of multi-wavelength observations for detailed studies of cluster astrophysics.

• Constraining Feedback Processes through the Sunyaev–Zeldovich Effect About 6% of CMB photons are Thomson-scattered by free electrons in the intergalactic medium (IGM) and intercluster medium (ICM), and a fraction of these are responsible for the thermal and kinetic Sunyaev–Zeldovich effects (tSZ and kSZ) [43, 44]. The amplitude of the tSZ is proportional to the integrated electron pressure along the line of sight, and it thus contains information about the thermodynamic properties of the IGM and ICM, which are highly sensitive to astrophysical feedback. With its low noise and broad frequency coverage, which is essential for separating out other signals, PICO will yield a definitive tSZ map over the full sky with a total SNR of 1270 for the CBE and 10% lower for the baseline configurations (Fig. ??). **what is unique? Full sky? frequencies? resolution?** The 150,000 clusters forecast to be detected by PICO will be found in this map. Considering the LSST gold weak-lensing sample, with a source density of 26 galaxies/arcmin² covering 40% of the sky, we forecast a detection of the tSZ–weak-lensing cross-correlation with SNR = 3000. Cross-correlations with the galaxies themselves will be measured at even higher SNR. At this immense significance, the signal will be broken down into dozens of tomographic redshift bins, precisely tracing the evolution of thermal pressure over cosmic time.

2.4 Testing Λ CDM

The current host of cosmological observations including the CMB fit within the Λ CDM model, but they have statistical strength to constrain only six of more than a dozen known cosmological parameters. A figure of merit (FOM) that quantifies the strength of the constraint is the volume of the uncertainty region in the N -dimensional parameter space [45–48].

Fig. 2.3 shows the increase in the FOM since *COBE* for the six-parameter Λ CDM model, as well as for additional cosmological parameters. The Figure only includes data from CMB experiments. The FOM for Λ CDM improved by a factor of 100 between *WMAP* and *Planck*, and will further improve by a factor of 10^5 with PICO. For the 11-parameter set that includes N_{eff} shown in the Figure PICO will improve upon *Planck* by a factor of 0.5×10^9 . Having achieved this improvement, there would be only little information left to extract with this parameter set even by a mission with double the resolution and nearly ten times lower noise (Fig. 2.3). Even stronger FOM improvements are obtained when a 12-parameter set is considered [49], and when the PICO CMB data will be combined with data sets available in the next decade, including weak lensing, BAO, and cluster of galaxies.

2.5 Galactic Structure and Star Formation

Planck enabled an immense step forward in Galactic astrophysics [50]. PICO will provide an even greater leap forward. It will produce 21 polarization maps of Galactic emission, and in the bands already probed by *Planck* they will be much deeper; for example, PICO’s map at 321 GHz will

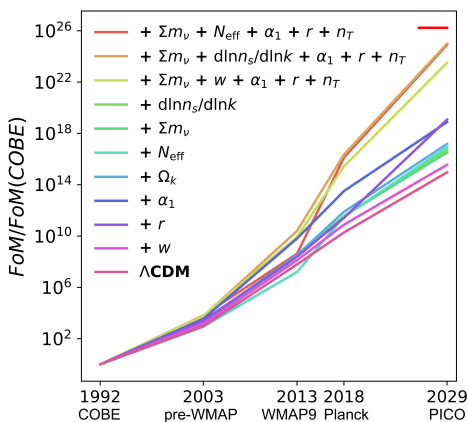


Figure 2.3: The increase in the FOM using data from CMB experiments since *COBE* for the Λ CDM six-parameter model (dark purple) and when adding other cosmological parameters. Increase in value represents increase in information content. PICO data will continue the average trend (blue line, Λ CDM + α_1) of doubling the FOM every 10 months since 1992. For an 11-parameter set that includes N_{eff} (red increasing line) PICO will improve the FOM by a factor of 0.5×10^9 relative to *Planck*, and will extract nearly the same information as that attainable by a mission with double the resolution and nine times lower baseline noise (top right red horizontal bar). The 11-parameter set includes: w -dark energy; r -the tensor to scalar ratio; α_1 -amplitude of correlated CDM isocurvature perturbations; Ω_k -curvature; N_{eff} -effective number of light relics; Σm_ν -sum of neutrino masses; and $d \ln n_s / d \ln k$ -running of the spectral index.

be 105 times deeper than *Planck*'s mean map depth at 353 GHz. At 799 GHz PICO will have five times the resolution of *Planck*'s highest resolution map (Fig. 2.4). Such a data set can only be obtained by PICO. These data will complement a rich array of other polarization observations forthcoming in the next decade, including stellar polarization surveys to be combined with Gaia astrometry, and Faraday rotation measurements from observations at radio wavelengths with the Square Kilometer Array (SKA) and its precursors.

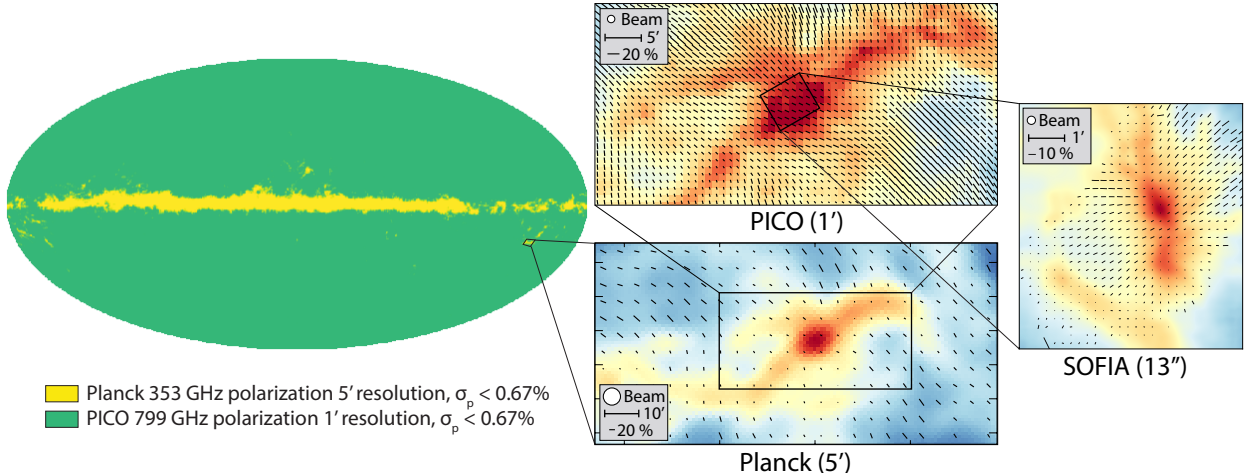


Figure 2.4: *Planck*'s 353 GHz polarization map gave a resolution of $5'$ and sensitivity to polarization intensity of $\sigma_p < 0.67\%$ over a small portion of the sky (left, yellow). At 799 GHz, the PICO baseline mission will give a polarization map of the *entire sky* and with 5 times higher resolution (left, green). In the middle panels, the *Planck* map of the Orion region overlaid with vectors that are aligned with the inferred magnetic field (lower panel), and a simulated PICO observation (upper panel) illustrate the leap in information content (vector lengths are proportional to polarization fraction). With this map, and maps at other frequencies, PICO will characterize Galactic magnetized turbulence at scales spanning the diffuse ISM down to dense star-forming cores, which will be mapped with high-resolution polarimetry by instruments such as HAWC+/SOFIA [51] (right panel) and ALMA [52].

While the PICO data will likely provide many new insights and surprises, we focus here on two particularly important science objectives: (1) Test models of the composition of interstellar dust, and (2) Determine how magnetic fields affect molecular cloud and star formation.

- **Test models of the composition of interstellar dust** Less than $1\,\mu\text{m}$ in size, dust grains are intermediate in the evolution from atoms and molecules to large solid bodies such as comets, asteroids, and planets. Through vastly improved spectral characterization of Galactic polarization, the PICO data will discriminate among models of Galactic dust composition to elucidate the chemical evolution of the Galaxy. For example, for the two-component paradigm [53], the PICO baseline mission will determine the intrinsic polarization fractions of each of the two components to a precision of 3%. With this level of precision the data will validate or reject state-of-the-art dust models [e.g. 54, 55], test for the presence of additional grain species with distinct polarization signatures, such as magnetic nanoparticles [56], and will be used as an input for the foreground separation necessary to extract cosmological E - and B -mode science.
- **Determine how magnetic fields affect molecular cloud and star formation** Stars are formed through interactions between gravitational and magnetic fields, turbulence, and gas over more than four orders of magnitude of spatial scales, which span the diffuse ISM (kpc scale), molecular clouds (10 pc), and molecular cloud cores (0.1 pc). However, the role magnetic fields play in the large-scale structure of the diffuse interstellar medium (ISM) and in the observed low star-formation efficiency has been elusive, owing to the dearth of data. With $1.1'$ resolution PICO will expand the number of independent magnetic field measurements across the sky by a factor of 2900, from *Planck*'s 30,000 to 86,000,000 (Fig. 2.4). The data will robustly characterize turbulent properties like the Alfvén Mach number, \mathcal{M}_A , across a previously unexplored regime of parameter space. With full-sky coverage, PICO will map all the molecular clouds out to a distance of 3.4 kpc with better than 1 pc resolution; we estimate there will be over 2,000 clouds that will be mapped with 10^3 – 10^5 independent polarization measurements per cloud. These are the *only foreseeable* measurements that will give the ratio of the energies stored in magnetic and gravitational fields, and the ratio of the energy stored in the magnetic field to that stored in gas turbulence over a statistically significant sample of molecular clouds.

2.6 Legacy Surveys

PICO was designed to respond to requirements posed by the seven science objectives (SOs) listed in Table ???. It will also generate a rich catalog of hundreds of thousands of new sources, consisting of proto-clusters, strongly lensed galaxies, and polarized radio and dusty galaxies. An abundance of information about galaxy and cluster evolution, dark matter, the physics of jets of active galactic nuclei, and magnetic fields of dusty galaxies will be stored in this catalog (Table 2.1). The catalog will be mined in future years through subsequent analysis and follow-up observations.

2.7 Signal Separation

2.7.1 The Signal Separation Challenge

Galactic emission dominates the sky's polarized intensity on large angular scales ($\ell \lesssim 10$), it dominates the cosmological B -modes signals for $\ell \lesssim 150$ for all allowed levels of r , and it is expected to be significant even at $\ell \simeq 1000$, posing challenge for reconstructing the B -mode signal from lensing. This is illustrated in Figs. ?? and 2.5, which show Galactic emission power spectra calculated for the cleanest – that is, the least Galactic-emission-contaminated – 60% of the sky. But even in small patches of the sky, far from the Galactic plane and with the least foreground contamination, Galactic emission levels are substantial relative to an inflationary signal of $r \sim 0.01$ [57]. Separating the cosmological and Galactic emission signals is one of two primary challenges facing any next-decade experiment attempting to reach these levels of constraints on r (the second is control

Table 2.1: Legacy Surveys

Catalog	Impact	Science
Strongly lensed galaxies	Discover 4500 ^a strongly lensed and highly magnified dusty galaxies across redshift. Current knowledge: 13 sources confirmed in <i>Planck</i> data; a few hundred candidates in <i>Herschel</i> , SPT and ACT data.	Gain information about the physics governing early, $z \simeq 5$, galaxy evolution, taking advantage of magnification and extra resolution enabled by gravitational lensing; learn about dark matter sub-structure in the lensing galaxies.
Proto-clusters	Discover 50,000 ^a mm/sub-mm proto-clusters distributed over the sky out to $z \sim 4.5$. Current knowledge: <i>Planck</i> + ACT/SPT data expected to yield a few tens.	Probe the earliest phases of cluster evolution, well beyond the reach of other instruments; test the formation history of the most massive virialized halos; investigate galaxy evolution in dense environments.
Nearby galaxies	Detect 30,000 galaxies at $z \lesssim 0.1$ at frequencies above 300 GHz. Current knowledge: 3400 (280) source candidates in the <i>Planck</i> 857 (353) GHz band.	Using frequencies that match cold (15 – 25 K) dust emission, give its spectral energy distribution as a function of galaxy properties to enable correlations with star-formation activity.
Polarized point sources	Detect 2000 ^b radio and several thousand dusty galaxies in polarization. Current knowledge: about 200 radio sources up to 100 GHz; one polarization measurement of a dusty galaxy.	Study the physics of jets of extragalactic sources, close to their active nuclei; determine the large-scale structure of magnetic fields in dusty galaxies; determine the importance of polarized sources as a foreground for CMB polarization science.
Cosmic infrared background	Provide eight maps of the anisotropy from dusty star-forming galaxies for frequencies $\nu > 200$ GHz, and with 1' resolution at 800 GHz. Current knowledge: Three <i>Planck</i> (higher noise) maps between 300 and 900 GHz with 5' resolution.	Improve constraints on the parameters describing universal star-formation history. Construct a tracer of large-scale structure for CMB de-lensing. Cross-correlate with galaxy surveys and CMB lensing map.

^a Confusion (not noise) limited

^b Noise and confusion limited

of systematic uncertainties).

To investigate the efficacy of PICO in addressing the foreground-separation challenge, we used both an analytic forecast and map-domain simulations; a complete description is given in Hanany et al. [58]. Here we present results only from the more conservative map-domain analysis. In this analysis we simulate sky maps that are constrained by available data, but otherwise have a mixture of foreground properties; we ‘observe’ these maps just like a realistic experiment would do, and then apply foreground separation techniques to separate the Galactic and CMB emissions. Our results indicate that:

- the combination of PICO’s sensitivity and broad frequency coverage are effective in foreground removal and that PICO will reach the requirement of $r = 5 \times 10^{-4}$ (5σ); see Figure 2.6;
- the high frequency bands, above 400 GHz, may be essential for proper subtraction of foregrounds; see Figure 2.7.

Among all next decade experiments, PICO is best suited to handle and model the foregrounds because it has more frequency bands than any other experiment, because it has the lowest noise, and because it has full sky coverage, giving access to several independent small regions that are very low in dust emission. This is a distinct advantage relative to CMB-S4, which targets a single

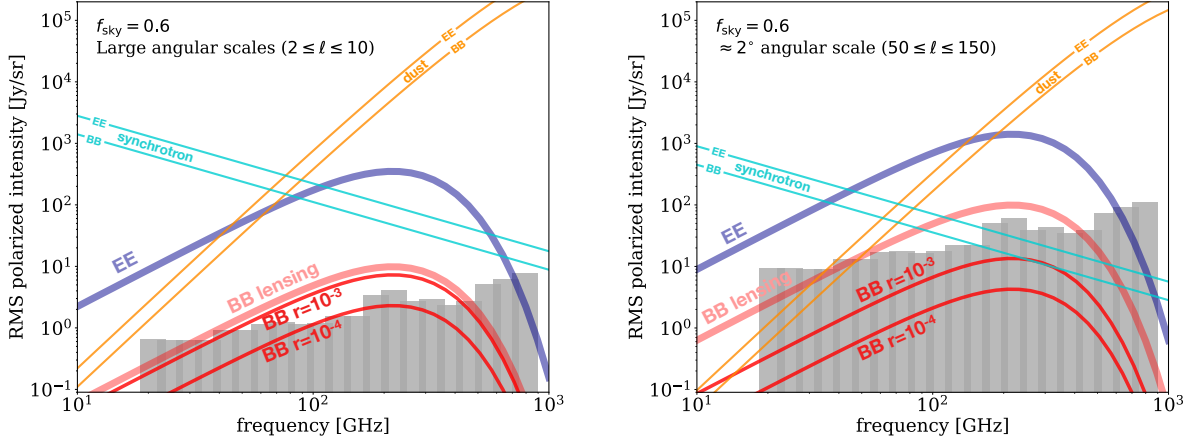


Figure 2.5: Polarization BB spectra of Galactic synchrotron and dust, compared to CMB polarization EE and BB spectra of different origins for two values of r and for two ranges of angular scales: large-scale, $\ell \leq 10$, corresponding to the reionization peak (left panel); and intermediate scales $50 \leq \ell \leq 150$, corresponding to the recombination peak (right panel). Data from *Planck* indicate that for Galactic emission the level of the E -mode is approximately twice that of B [57]. The PICO baseline noise (grey bands) is low compared to the Galactic emission components, and thus they will be measured with high SNR in many frequency bands.

patch of the sky, and relative to liteBIRD, which does not have frequency bands above 400 GHz.

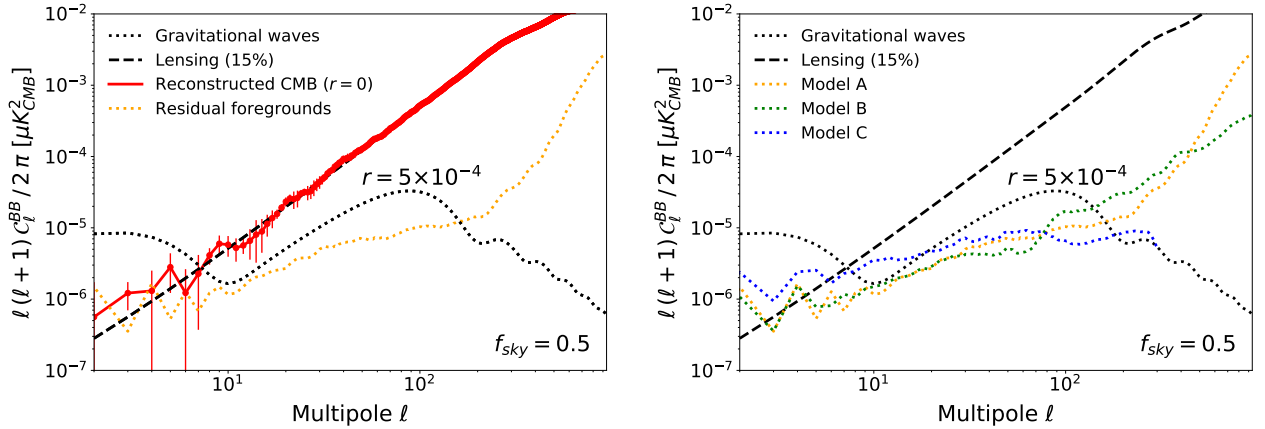


Figure 2.6: Angular power spectra of BB due to the CMB and of residual foregrounds after an end-to-end map-based foreground-separation exercise. The PICO low noise levels and breadth in frequency coverage enable separation of model A foregrounds such that the residual foreground spectrum (left, yellow dotted) is a factor of ten (four) below a BB inflationary signal with $r = 5 \times 10^{-4}$ (black dotted) at $\ell = 5(80)$. Within errors, the recovered CMB (red) matches the input CMB, which consists of only lensing BB (dashed black), over all angular scales $\ell \gtrsim 6$. The results for model B are similar (right, green dots), while model C has somewhat higher residuals at low ℓ . In this exercise we used 50% of the sky. Lower foreground residual levels are obtainable with smaller, cleaner patches of $\sim 5\%$ of sky, which would reduce the residual foregrounds at $\ell \simeq 80$.

2.8 Systematic Uncertainties

Properly modeling, engineering for, and controlling systematic effects are key for the success of any experimental endeavor striving to achieve $\sigma(r) \lesssim 1 \times 10^{-3}$. Based on extensive community experience with both hardware and analysis of data we make the following points.

- Relative to other platforms, a space-based mission provides the most thermally stable platform,

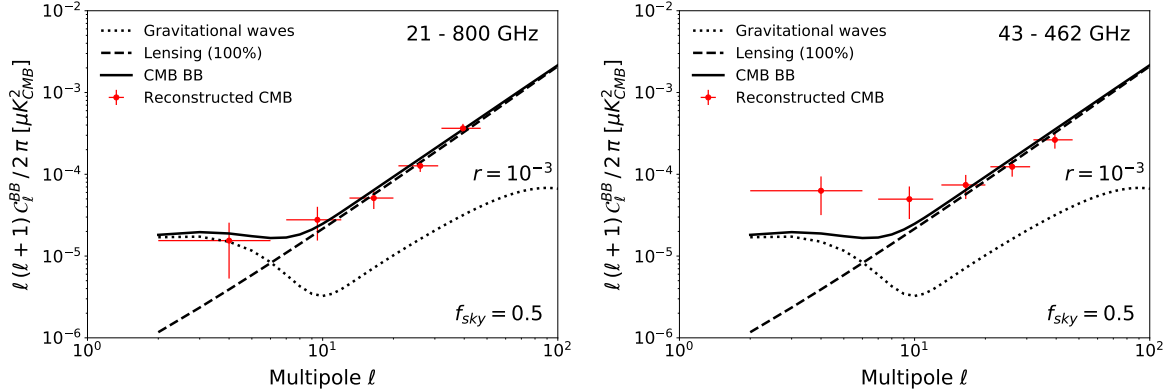


Figure 2.7: **Left:** Foreground separation with all of PICO’s 21 frequency bands recovers the input CMB *BB* power spectrum (solid black) without bias (red). The input CMB spectrum has a contribution from lensing (dashed) and an inflationary signal with $r = 0.001$ (dotted). This exercise uses a parametric approach [59] with foregrounds varying on 4° pixels, and using 50% sky fraction. **Right:** Running the same foreground separation algorithm on the same sky but using only PICO’s bands between 43 and 462 GHz produces an output spectrum (red) that is biased at low multipoles relative to the input. With real data, such a bias would be erroneously interpreted as a higher value of r .

and thus the prerequisite for improved control of systematic effects. PICO’s orbit at L2 is among the most thermally stable of possible orbits.

- PICO’s sky scan pattern gives strong data redundancy, which enables numerous cross-checks. Each of the 12,996 detectors makes independent maps of the I , Q , and U Stokes parameters enabling many comparisons within and across frequency bands, within and across sections of the focal plane, and within and across bolometers that have either the same or different polarization sensitivities. Half the sky is scanned every two weeks, and the entire sky is scanned in 6 months. Thus combinations of maps constructed at different times during of the mission will be differenced to search for residual time-dependent systematic effects.
- The scan pattern gives almost continuous scans of planets and large amplitude (≥ 4 mK) CMB dipole signals [60]. These features result in continuous, high SNR calibration and antenna-pattern characterization. In comparison, *Planck* observed each of the planets with only a 6 month cadence and had nearly 100 days/year during which the dipole calibration signals were below 4 mK, at times dipping below 1 mK.
- We showed that two of the highest priority systematic effects can be controlled to levels that are small compared to requirements. More analysis and planning is required to address systematic uncertainties arising from the far-sidelobe response of the telescope.

We direct the reader to the mission study report for more details on our work on systematic effects for PICO [58].

2.9 Complementarity with Sub-Orbital Measurements

Since the first CMB measurements, more than 50 years ago, important observations have been made from the ground, from balloons, and from space. Each of the CMB satellites flown to date – *COBE*, *WMAP*, and *Planck* – has relied on technologies and experience that were the result of sub-orbital efforts. PICO is no different. Examples include: the arrays of micro-fabricated, multi-color pixels and the multiplexed readout that are baselined for the PICO focal plane are a consequence of this decade’s technical developments (§ 3.2, § 3.3); and the recent results from *Planck* and ground-based experiments that established the need for a multitude of frequency bands to characterize and

Table 2.2: Relative characteristics of ground, balloon, and space platforms for experiments in the CMB bands.

Characteristic	Ground	Balloon	Space
Sky coverage	Partial from single site	Partial from single flight	Full
Frequency coverage	70 GHz inaccessible, ^a $\nu \geq 300$ GHz unusable, limited atmospheric windows	70 GHz inaccessible, ^a otherwise, almost unlimited	Unrestricted
Angular resolution at 150 GHz ^b	1. ⁵ with 6 m telescope	6' with 1.5 m telescope	6' with 1.5 m telescope
Detector noise ^c	$265 \mu\text{K}_{\text{CMB}} \sqrt{\text{s}}$	$162 \mu\text{K}_{\text{CMB}} \sqrt{\text{s}}$	$38 \mu\text{K}_{\text{CMB}} \sqrt{\text{s}}$
Integration time	Unlimited, with interruptions	Weeks, continuous	Several years, continuous
Repairability, Upgradeability ...	Good	None; multiple flights possible	None

^a 70 GHz is the frequency at which large angular scale B -mode Galactic emissions have a minimum (Fig. 2.5).

^b We give representative telescope apertures. Significantly larger apertures for balloons and in space result in higher mass, volume, and cost.

^c The noise-equivalent temperatures given are illustrative of general capabilities. Detailed comparisons depend on detector heat-sink temperatures, bandwidths, and other factors that differ among specific implementations. Ground – median detector noise at 95 GHz from BICEP3 [61]; balloon – median detector noise at 94 GHz from SPIDER [62]; space – 90 GHz from PICO CBE.

control foregrounds. A healthy sub-orbital program is essential for the success of PICO.

The phenomenal success and the immense science outcomes of past space missions are a direct consequence of their relative advantages (Table 2.2). In every respect, with the exception of repairability and upgradeability, space has the advantage. When the entire sky is needed, as for measurements on the largest angular scales, space is by far the most suitable platform. When broad frequency coverage is needed, space will be required to reach the ultimate limits set by astronomical foregrounds because ground-based observations are limited to a handful of atmospheric windows, mostly below 300 GHz. Balloons can provide useful information at higher frequencies, but their limited observing time limits SNR. The stability offered in space can not be matched on any other platform, and it translates to superb control of systematic uncertainties.

The relative advantages of a space mission used to come with higher costs relative to sub-orbital experiments. However, this balance now shifts. To make further advances in CMB science it is now required to mount massive ground-based efforts. By the early 2020s, S3 experiments plan to implement more than 100,000 detectors in 9 receivers in Chile and the South Pole. The total cost is in the vicinity of \$100M. The cost for a subsequent scale-up, a \sim 500,000-detector ground-based CMB experiment planned for the next decade, is squarely within the cost window of this Probe. Even at that cost, the PICO goal of reaching $r = 5 \times 10^{-4}$ (5σ) is beyond the reach of sub-orbital observations in the foreseeable future.

For measuring r and for achieving the other PICO SOs, a space-based platform is either necessary or has strong advantages. For science requiring higher angular resolution, such as observations of galaxy clusters with 1 arcmin resolution at 150 GHz, the ground has an advantage. An appropriately large aperture on the ground will also provide high-resolution information at lower frequencies, which may be important for separating Galactic emissions at high ℓ . We therefore recommend to pursue a space mission in the next decade, and to complement it with a ground-based program that will overlap in ℓ space, and will add science at the highest angular resolution, beyond the reach of a space mission.

Balloon observations have been exceedingly valuable in the past, and will continue to play an

important role through making measurements at frequency bands above 280 GHz. Because balloon observations are largely free from the noise induced by atmospheric turbulence, they are suited for probing the low ℓ multipoles. The balloon environment is the best available for elevating the TRL of relevant technologies.

3 Technical Overview

PICO meets all of its science-derived instrument requirements (§ ??) with a single instrument: an imaging polarimeter with 21 logarithmically spaced frequency bands centered between 21 and 799 GHz (Table ??). The instrument has a two-reflector Dragone-style telescope (§ 3.1 and Fig. 3.1). The focal plane is populated by 12,996 transition-edge-sensor (TES) bolometers (§ 3.2) and read out using a time-domain multiplexing scheme (§ 3.3). PICO employs a single science observing mode: fixed rate imaging while scanning the sky (§ 4.1.2).

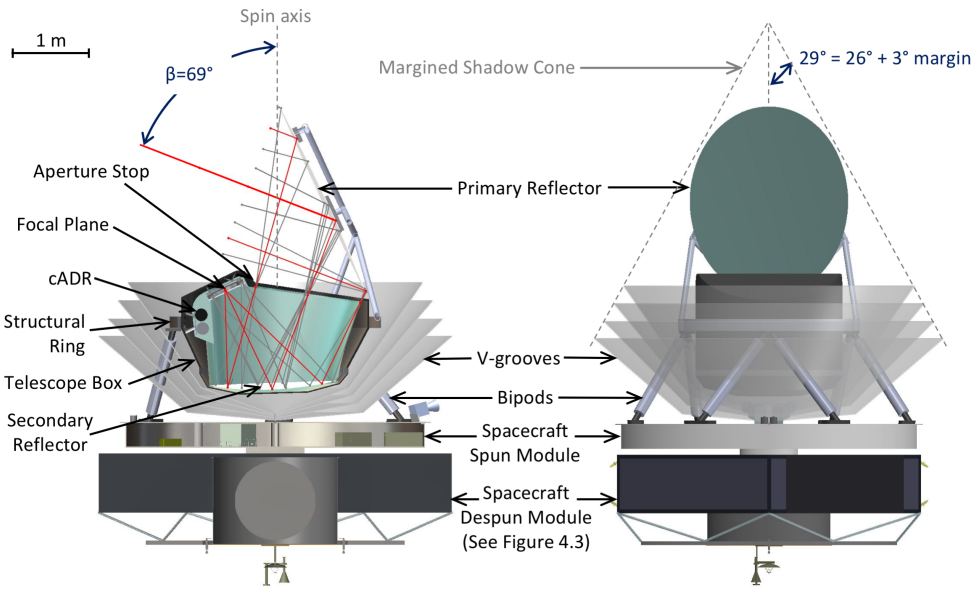


Figure 3.1: PICO overall configuration in side view and cross section (left), and front view with V-Groove assembly shown semi-transparent (right). The mission consists of a single science instrument mounted on a structural ring. The ring is supported by bipods on a stage spinning at constant speed relative to a despun module. Figure 3.2 shows the functions hosted by each of the modules.

The instrument is configured inside the shadow of a V-groove assembly that thermally and optically shields it from the Sun (Fig. 3.1 and § 3.4.3). The Sun shadow cone depicted in Fig. 3.1 is 29° . The angle to the Sun during the survey, $\alpha = 26^\circ$ (§ 4.1.2 and Fig. 4.2), is supplemented with a margin of 3° to account for the radius of the Sun ($0^\circ 25$), pointing control error, design margin, and alignment tolerances.

The V-groove assembly is attached to the bipod struts that support the instrument structural ring. The ring supports the primary reflector and telescope box. The telescope box contains the actively cooled components (§ 3.4.1, § 3.4.2), including the secondary reflector, the focal plane and sub-kelvin refrigerator structures. Just inside the box, a thermal liner serves as a cold optical baffle and aperture stop. Instrument integration and test are described in § 3.5.

During the survey, the instrument is spun at 1 rpm and the spin axis is made to precess about the anti-Sun direction (§ 4.1.2). Spacecraft control is simplified by mounting the instrument on a spinning spacecraft module, while a larger non-spinning module houses most spacecraft subsystems

(§ 4.3). Instrument elements that act as heat sources are accommodated on the spinning module of the spacecraft. Only power and digital data lines cross between the spinning and non-spinning modules. A functional block diagram of the instrument is shown in Figure 3.2.

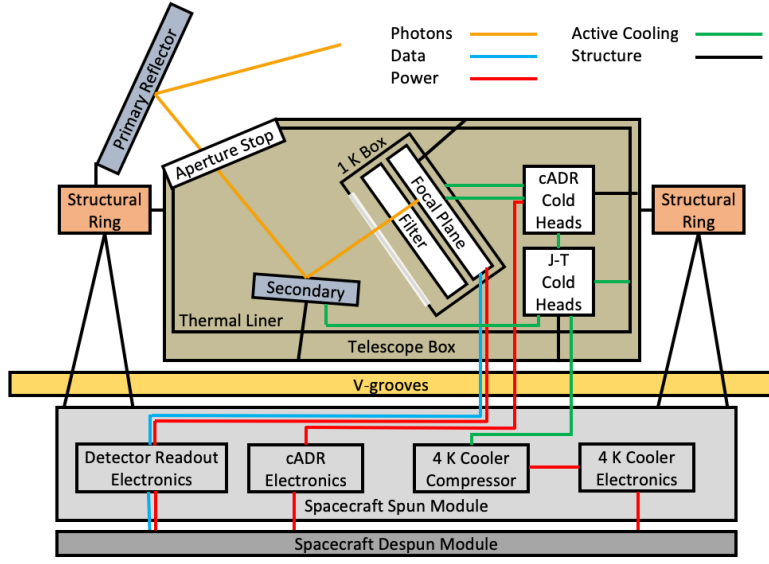


Figure 3.2: PICO instrument block diagram. Active coolers provide cooling to the 100 mK focal plane, the surrounding 1 K box, the 4.5 K secondary reflector, and the 4.5 K thermal liner that acts as a cold aperture stop. V-grooves provide passive cooling. The instrument, V-grooves, and spacecraft spun module spin together at a rate of 1 RPM. The spacecraft spun module hosts the 4 K cooler compressor and drive electronics, the sub-K cooler drive electronics, and the detector warm readout electronics. Only power and digital data lines cross to the spacecraft despun module, which hosts the spacecraft power, telemetry, attitude control, and communication systems (§ 4.3).

3.1 Telescope

The PICO telescope design is driven by a combination of science requirements and physical volume limits. The science requirements are: a large diffraction-limited field of view (DLFOV) sufficient to support approximately 10^4 detectors; arcminute resolution at 800 GHz; low spurious polarization; and low sidelobe response. All requirements are met with PICO’s 1.4 m aperture modified open-Dragone design. There are no moving parts in the PICO optical system.

The PICO optical design was selected following a trade study examining cross-Dragone, Gregorian Dragone, and open-Dragone designs [63]. The open-Dragone and crossed-Dragone systems offer more diffraction-limited focal-plane area than the Gregorian Dragone one [64] and are able to support enough detectors to provide the required sensitivity. The open-Dragone design does not require the more massive and voluminous baffles that the cross-Dragone does, and hence can satisfy the aperture size requirement within the shadow cone.

PICO’s initial open-Dragone design [65, 66] has been modified with the addition of an aperture stop and adding corrections to the primary and secondary reflectors to enlarge the DLFOV. The detailed geometric parameterization of the PICO optical design is described by Young et al. [63]. The primary reflector ($270 \text{ cm} \times 205 \text{ cm}$) is passively cooled and the secondary reflector ($160 \text{ cm} \times 158 \text{ cm}$) is actively cooled. The highest frequency (900 GHz) sets the surface accuracy requirement of the reflectors at $\lambda/14 = 24 \mu\text{m}$. The focal ratio is 1.42. The slightly concave focal surface, which has a radius of curvature of 4.55 m, is telecentric to within 0.12° across the entire FOV.

An actively cooled circular aperture stop between the primary and secondary reflectors reduces detector noise and shields the focal plane from stray radiation. Stray-light analysis of the PICO open-Dragone design using GRASP confirms that the focal plane is protected from direct view of

the sky, and that spillover past the primary is suppressed by 80 dB relative to the main lobe for both co-pol and cross-pol beams. Detailed baffle design will be performed during mission formulation.

3.2 Focal Plane

PICO’s focal plane is populated by an array of TES bolometers operating in 21 frequency bands, each with 25% fractional bandwidth, and band centers ranging from 21 to 799 GHz. The layout of the PICO focal plane is shown in Fig. 3.3 and detailed in Table 3.1.

Bolometers operating in the mm/sub-mm wave band are photon-noise limited. Therefore, increase in sensitivity is achieved through an increase in detector count. The PICO focal plane has 12,996 detectors, 175 times the number flown aboard *Planck*, thereby providing a breakthrough increase in sensitivity

with a comparably sized telescope. This breakthrough is enabled by development and demonstration in suborbital projects, which now commonly operate arrays of $10^3\text{--}10^4$ detectors (§ 5). Further technology maturation required for PICO is described in Section § 5.

3.2.1 21–462 GHz Bands

Several optical-coupling technologies have matured over the past ten years to efficiently use focal-plane area: horns with ortho-mode transducers (OMTs) [67]; lithographed antenna arrays [68]; and sinuous antennas under lenslets [69]. Horn-coupling and sinuous antenna/lenslet-coupling deliver quantum efficiency $> 70\%$ over more than an octave of bandwidth, which have been partitioned into two or three colors per pixel. Only single-color pixels have been demonstrated to date with antenna-arrays, but this coupling enables smaller pixels and therefore they can be more densely packed.

The PICO baseline focal plane employs three-color sinuous antenna/lenslet pixels [70] for the 21–462 GHz bands. Niobium microstrips mediate the signals between the antenna and detectors, and partition the wide continuous bandwidth into three narrow channels using integrated, on-wafer, micro-machined filter circuits [71]. Six transition edge sensor bolometers per pixel detect the radiation in two orthogonal polarization states.

3.2.2 555–799 GHz Bands

PICO’s highest three frequency channels are beyond the niobium superconducting band-gap, rendering on-wafer, microstrip filters a poor solution for defining the optical passband. For these bands we use feedhorns to couple the radiation to two single-color

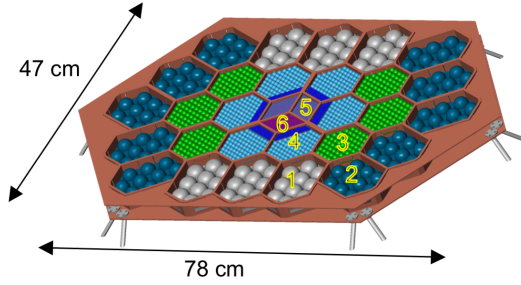


Figure 3.3: PICO focal plane. Detectors are fabricated on six types of tiles (shown numbered and colored as in Table 3.1). The wafers are located on the focal plane such that higher frequency bands, which require better optical performance, are placed nearer to the center. All detectors are within the diffraction-limited performance for their respective frequency bands.

Figure 3.3: PICO focal plane. Detectors are fabricated on six types of tiles (shown numbered and colored as in Table 3.1). The wafers are located on the focal plane such that higher frequency bands, which require better optical performance, are placed nearer to the center. All detectors are within the diffraction-limited performance for their respective frequency bands.

Table 3.1: PICO makes efficient use of the focal area with multichroic pixels (three bands per pixel, § 3.2.1). The sampling rate is based on the smallest beam (Table 3.2), with 3 samples per FWHM at a scan speed ($360^\circ/\text{min}$) $\sin(\beta = 69^\circ) = 336^\circ/\text{min}$. Scaling from suborbital experience, we anticipate that TES bolometers can support these sampling rates with $\sim 4\times$ margin.

Tile type	N_{tile}	Pixels/tile	Pixel type	Band centers [GHz]	Sampling rate [Hz]
1	6	10	A	21, 30, 43	45
2	10	10	B	25, 36, 52	55
3	6	61	C	62, 90, 129	136
4	6	85	D	75, 108, 155	163
		80	E	186, 268, 385	403
5	2	450	F	223, 321, 462	480
6	1	220	G	555	917
		200	H	666	
		180	I	799	

Table 3.2: PICO has 21 partially overlapping frequency bands with band centers (v_c) from 21 GHz to 799 GHz and each with bandwidth $\Delta v/v_c = 25\%$. The beams are single mode, with FWHM sizes of $6.2 \times (155 \text{ GHz}/v_c)$. The CBE per-bolometer sensitivity is photon-noise limited (§ 3.2.4). The total number of bolometers for each band is equal to (number of tiles) \times (pixels per tile) \times (2 polarizations per pixel), from Table 3.1. Array sensitivity assumes 90% detector operability. The map depth assumes 5 yr of full sky survey at 95% survey efficiency, except the 25 and 30 GHz frequency bands, which are conservatively excluded during 4 hr/day Ka-band (26 GHz) telecom periods (§ 4.2).

Band center	Beam FWHM	CBE bolo NET	N_{bolo}	CBE array NET	Baseline array NET	Baseline polarization map depth	
[GHz]	[arcmin]	$[\mu\text{K}_{\text{CMB}} \text{s}^{1/2}]$		$[\mu\text{K}_{\text{CMB}} \text{s}^{1/2}]$	$[\mu\text{K}_{\text{CMB}} \text{s}^{1/2}]$	$[\mu\text{K}_{\text{CMB}} \text{arcmin}]$	$[\text{Jy sr}^{-1}]$
21.....	38.4	112	120	12.0	17.0	23.9	8.3
25.....	32.0	103	200	8.4	11.9	18.4	10.9
30.....	28.3	59.4	120	5.7	8.0	12.4	11.8
36.....	23.6	54.4	200	4.0	5.7	7.9	12.9
43.....	22.2	41.7	120	4.0	5.6	7.9	19.5
52.....	18.4	38.4	200	2.8	4.0	5.7	23.8
62.....	12.8	69.2	732	2.7	3.8	5.4	45.4
75.....	10.7	65.4	1020	2.1	3.0	4.2	58.3
90.....	9.5	37.7	732	1.4	2.0	2.8	59.3
108.....	7.9	36.2	1020	1.1	1.6	2.3	77.3
129.....	7.4	27.8	732	1.1	1.5	2.1	96.0
155.....	6.2	27.5	1020	0.9	1.3	1.8	119
186.....	4.3	70.8	960	2.0	2.8	4.0	433
223.....	3.6	84.2	900	2.3	3.3	4.5	604
268.....	3.2	54.8	960	1.5	2.2	3.1	433
321.....	2.6	77.6	900	2.1	3.0	4.2	578
385.....	2.5	69.1	960	2.3	3.2	4.5	429
462.....	2.1	133	900	4.5	6.4	9.1	551
555.....	1.5	658	440	23.0	32.5	45.8	1580
666.....	1.3	2210	400	89.0	126	177	2080
799.....	1.1	10400	360	526	744	1050	2880
Total		12 996		0.43	0.61	0.87	

polarization-sensitive TES bolometers. The waveguide cut-off defines the lower edge of the band, and quasi-optical metal-mesh filters define the upper edge. Numerous experiments have successfully used similar approaches [72–74].

3.2.3 Polarimetry

Polarimetry is achieved by differencing the signals from pairs of two co-pointed bolometers within a pixel that are sensitive to two orthogonal polarization states. Half the pixels in the focal plane are sensitive to the Q and half to the U Stokes parameters of the incident radiation. Two layouts for the distribution of the Q and U pixels on the focal plane have been investigated [75]; both would satisfy mission requirements. Stokes I is obtained from the sum of the signals of orthogonal detectors.

3.2.4 Sensitivity

PICO’s Current Best Estimate (CBE) sensitivity meets the requirements of the baseline mission with > 40 % margin (Table 3.2).

We developed an end-to-end noise model of the PICO instrument to predict mission sensitivity and provide a metric by which to evaluate mission design trades. The model includes four noise sources per bolometer: photon, phonon, Johnson, and readout (from both cold and warm readout electronics). To validate our calculations, we compared two independent software packages that have been validated with several operating CMB instruments. The calculations agreed within 1% both for individual noise terms and for overall mission noise. A detailed description of the PICO noise model and its inputs is available in Young et al. [63]; small differences between that publication and Table 3.2 are due to refinements of the primary mirror and stop temperatures.

Laboratory experiments have demonstrated that TES bolometers can be made background-limited in the low loading environment they would experience at L2 [76]. For PICO, the primary contributor to noise is the optical load. The sources of optical load are the CMB, reflectors, aperture stop, and low-pass filters. The CMB and stop account for at least 50% of the optical load at all frequencies up to and including 555 GHz. At higher bands emission from the primary mirror dominates.

The sensitivity model assumes white noise at all frequencies. Sub-orbital submillimeter experiments have demonstrated TES detectors that are stable to at least as low as 20 mHz [77], meeting the requirements for PICO’s scan strategy (§ 4.1.2).

3.3 Detector Readout

Suborbital experiment teams over the past ten years have chosen to use voltage-biased TESs because their current readout scheme lends itself to superconducting quantum interface device (SQUID)-based multiplexing. Multiplexing reduces the number of wires to the cryogenic stages and thus the total thermal load that the cryocoolers must dissipate. This approach also simplifies the instrument design.

In the multiplexing circuitry, SQUIDs function as low-noise amplifiers and cryogenic switches. The current baseline for PICO is to use a time-domain multiplexer (TDM), which assigns each detector’s address in a square matrix of simultaneously read columns, and sequentially cycles through each row of the array [78]. The PICO baseline architecture uses a matrix of 128 rows and 102 columns. The thermal loading on the cold stages from the wire harnesses is subdominant to conductive loading through the mechanical support structures.

Because SQUIDs are sensitive magnetometers, suborbital experiments have developed techniques to shield them from Earth’s magnetic field using highly permeable or superconducting materials [79]. Total suppression factors better than 10^7 have been demonstrated for dynamic magnetic fields [80]. PICO will use these demonstrated techniques to shield SQUID readout chips from the ambient magnetic environment, which is 20,000 times smaller than near Earth, as well as from fields generated by on-board components, including the 0.1 K cooler (§ 3.4.1). This cooler is delivered with its own magnetic shielding, which reduces the field at the distance of the SQUIDs to less than 0.1 G, which is less than Earth’s field experienced by SQUIDs aboard suborbital experiments. SQUIDs are also sensitive to radio-frequency interference (RFI). Several suborbital experiments have demonstrated RFI shielding using aluminized mylar wrapped at cryogenic stages to form a Faraday cage around the SQUIDs [81–83]. Cable shielding extends the Faraday cage to the detector warm readout electronics.

Table 3.3: Projected cooler heat lift capabilities offer more than 100 % heat lift margin, complying with cooler technology best practices [87].

Component	Temperature [K]		Active heat lift [mW]		
	Required	CBE	Required per model ^a	Capability today	Projected capability
Primary reflector	< 40	17	N/A (radiatively cooled)		
Secondary reflector	< 8	4.5			
Aperture stop	4.5	4.5	42 at 4.5 K	> 55 at 6.2 K ^b	> 100 at 4.5 K ^c
cADR heat rejection ^d	4.5	4.5			
Focal plane enclosure and filter	1.0	1.0	0.36	1.0	N/A ^e
Focal plane	0.1	0.1	5.7×10^{-3}	32×10^{-3}	N/A ^e

^a The required loads were calculated using Thermal Desktop. Reference [88] was used to estimate the thermal conductive loads through mechanical supports. In addition to the listed components, the total 4.5 K heat load includes the intercept on the focal plane mechanical supports. ^b Reference [89]. ^c Both NGAS and Ball project > 100 mW

lift capability at 4.5 K using higher compression-ratio compressors currently in development (§ 3.4.2 and Fig. 3.4).

^d The cADR lift capability at 1 K and 0.1 K is from a GSFC quote. ^e Capability today already exceeds requirement.

Redundant warm electronics boxes perform detector readout and instrument housekeeping using commercially available radiation-hardened analog-to-digital converters, requiring 75 W total. The readout electronics compress the data before delivering them to the spacecraft, requiring an additional 15 W. PICO detectors produce a total of 6.1 Tbits/day assuming 16 bits/sample, sampling rates from Table 3.1, and bolometer counts from Table 3.2. *Planck* HFI had a typical 4.7× compression in flight, with information loss increasing noise by only about 10% [84, 85]. Suborbital work has demonstrated 6.2× lossless compression [86]. PICO assumes 4× lossless compression.

3.4 Thermal

Like the *Planck*-HFI instrument, PICO’s focal plane is maintained at 0.1 K to ensure low detector noise while implementing readily available technology (§ 3.4.1). To minimize detector noise due to instrument thermal radiation, the aperture stop and reflectors are cooled using both active and radiative cooling (§ 3.4.2, § 3.4.3, Fig. 3.2). All thermal requirements are met with robust margins (Table 3.3).

3.4.1 cADR Sub-Kelvin Cooling

A multi-stage continuous adiabatic demagnetization refrigerator (cADR) maintains the PICO focal plane at 0.1 K and the surrounding enclosure, filter, and readout components at 1 K. The cADR employs three refrigerant assemblies operating sequentially to absorb heat from the focal plane at 0.1 K and reject it to 1 K. Two additional assemblies, also operating sequentially, absorb this rejected heat at 1 K, cool other components to 1 K, and reject heat at 4.5 K. This configuration provides continuous cooling with small temperature variations at both the 0.1 K and 1 K. Heat straps connect the two cADR cold sinks to multiple points on the focal-plane assembly, which has high thermal conductance paths built in, to provide spatial temperature uniformity and stability during operation. The detector arrays are thermally sunk to the mounting frame. Heat loads in the range of 30 μ W at 0.1 K and 1 mW at 1 K (time-average) are within the capabilities of current cADRs developed by GSFC (§ 7.1) [90, 91]. The PICO sub-kelvin heat loads are estimated at less

than half of this capability (Table 3.3).

3.4.2 The 4.5 K Cooler

A cryocooler system similar to that used on JWST to cool the MIRI detectors [92, 93] removes the heat rejected from the cADR and cools the aperture stop and secondary reflector to 4.5 K. Both NGAS (which provided the MIRI coolers) and Ball Aerospace have developed such coolers under the NASA-sponsored Advanced Cryocooler Technology Development Program [94]. NGAS and Ball use slightly different but functionally-equivalent hardware approaches. A 3-stage precooler provides 16 K precooling to a separate circulated-gas loop. The circulated-gas loop utilizes Joule–Thomson (J-T) expansion, further cooling the gas to 4.5 K. The J-T expansion point is located close to the cADR heat rejection point and provides to it the lowest temperature. Subsequently, the gas flow intercepts heat conducted to the focal-plane enclosure, then cools the aperture stop and the secondary reflector before returning to the circulation compressor.

NGAS and Ball are actively working on increasing the flow rate and compression ratio of the J-T compressor, which should result in higher system efficiency and greater heat-lift relative to the current MIRI cooler. NGAS uses ^4He as the circulating gas, as was used for MIRI. Ball uses a somewhat larger compressor and ^3He as the circulating gas. Both employ re-optimized heat exchangers. The NGAS project has completed PDR-level development, and is expected to reach CDR well before PICO begins Phase-A. The projected performance of this cooler is shown in Fig. 3.4; it gives 100 mW at 250 W input power, which is more than 100 % heat lift margin relative to PICO’s requirements (Table 3.3). For PICO we have assumed an input power of 350 W.

The entire precooler assembly and the J-T circulator compressor are located on the warm spacecraft spun module (Fig. 3.2). All waste heat rejected by the cooler compressors and drive electronics is transferred to the spacecraft heat-rejection system. Unlike JWST, the PICO cooler does not require deployment of the remote cold head.

3.4.3 Radiative Cooling

An assembly of four nested V-groove radiators, acting as radiation shields, provides passive cooling (Fig. 3.1). This is standard, 30-years old technology (§ 7.1). The outermost shield shadows the interior ones from the Sun. The V-grooves radiate to space, each reaching successively cooler temperatures. The assembly provides a cold radiative environment to the primary reflector, structural ring, and telescope box. As a consequence radiative loads on those elements are smaller than the conductive loads through the mechanical support structures.

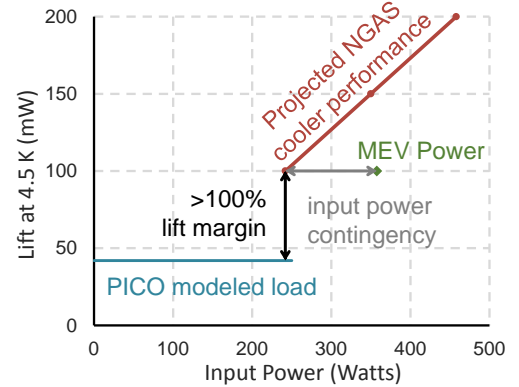


Figure 3.4: Projected performance of the NGAS cooler using a multi-stage compressor and ^4He circulating gas [92] meets PICO’s requirements with $> 100\%$ margin. PICO requires heat lift of 42 mW at 4.5 K (Table 3.3). With 250 W of input power the NGAS cooler is projected to provide 100 mW of heat lift. We conservatively specify a maximum expected value (MEV) of 350 W as the compressor’s input power, giving 100 W of additional input power contingency.

3.5 Instrument Integration and Test

The PICO instrument integration and testing plan benefits from heritage and experience with the *Planck* HFI instrument [95].

We screen detector wafers prior to selection of flight wafers and focal-plane integration. The cADR and 4 K cryocooler vendors will qualify them prior to delivery. We will determine the relative alignment of the two reflectors under in-flight thermal conditions using a thermal vacuum (TVAC) chamber and photogrammetry. We integrate the flight focal-plane assembly and flight cADR in a dedicated sub-kelvin cryogenic testbed. We characterize noise, responsivity, and focal-plane temperature stability using a representative optical load for each frequency band (temperature-controlled blackbody), and we perform polarimetric and spectroscopic calibration.

The focal plane is integrated with the reflectors and structures, and alignment verified with photogrammetry at cold temperatures in a TVAC chamber. The completely integrated observatory (instrument and spacecraft bus) is tested in TVAC to measure parasitic optical loading from the instrument, noise, microphonics, and RFI. The observatory is 4.5 m in diameter and 6.1 m tall. There are no deployables.

4 Design Reference Mission

The PICO design reference mission is summarized in Table 4.1.

Table 4.1: PICO carries margin on key mission parameters. Maximum Expected Value (MEV) includes contingency.

4.1 Concept of Operations

The PICO concept of operations is similar to that of the successful *WMAP* [96] and *Planck* [97] missions. After launch, PICO cruises to a quasi-halo orbit around the Earth–Sun L2 Lagrange point (§ 4.1.1). A two-week decontamination period is followed by instrument cooldown, lasting about two months. After in-orbit checkout is complete, PICO begins its science survey.

Orbit type	Sun-Earth L2 Quasi-Halo
Mission class	Class B
Mission duration	5 years
Propellant (hydrazine).....	213 kg (77 % tank fill)
Launch mass (MEV)	2147 kg (3195 kg capability)
Max power (MEV)	1320 W (with 125 % margin on available solar array area)
Onboard data storage	4.6 Tb (3 days of compressed data, enabling retransmission)

Survey implementation Instrument on spin table

PICO has a single science observing mode, surveying the sky continuously for five years using a pre-planned repetitive survey pattern (§ 4.1.2). Instrument data are compressed and stored on-board, then returned to Earth in daily 4-hr Ka-band science downlink passes (concurrent with science observations). Because PICO is observing relatively static Galactic, extragalactic, and cosmological targets, there are no requirements for time-critical observations or data latency. Presently, there are no plans for targets of opportunity or guest observer programs during the prime mission. The PICO instrument does not require cryogenic consumables (as the *Planck* mission did), permitting consideration of significant mission extension beyond the prime mission.

4.1.1 Mission Design and Launch

The science survey is conducted from a quasi-halo orbit around the Earth–Sun L2 Lagrange point. *Planck* and *WMAP* also operated in L2 orbits. L2 orbits provide favorable survey geometry relative to Earth orbits by mitigating viewing restrictions imposed by terrestrial and lunar stray light. The PICO orbit around L2 is small enough to ensure that the Sun–Probe–Earth (SPE) angle is less

than 15° . This maintains the telescope boresight $> 70^\circ$ away from the Earth (Fig. 4.2, $70^\circ = 180^\circ - \alpha - \beta - \text{SPE}$).

High data-rate downlink to the Deep Space Network (DSN) is available from L2 using near-Earth Ka bands. L2 provides a stable thermal environment, simplifying thermal control. The PICO orbit exhibits no post-launch eclipses.

NASA requires that Probes be compatible with an Evolved Expendable Launch Vehicle (EELV). For the purpose of this study, the Falcon 9 [98] is used as the reference vehicle. Figure 4.1 shows PICO configured for launch in a Falcon 9 fairing. The Falcon 9 launch capability for ocean recovery exceeds PICO’s 2147 kg total launch mass (including contingency) by a 50 % margin.

Insertion to the halo manifold and associated trajectory correction maneuvers require 150 m s^{-1} of total ΔV by the spacecraft. Orbit maintenance requires minimal propellant (statistical $\Delta V \sim 2 \text{ m s}^{-1} \text{ year}^{-1}$). The orbital period is ~ 6 months. There are no disposal requirements for L2 orbits, but spacecraft are customarily decommissioned to heliocentric orbit.

4.1.2 Survey Design

PICO employs a highly repetitive scan strategy to map the full sky. During the survey, PICO spins with a period $T_{\text{spin}} = 1 \text{ min}$ about a spin axis oriented $\alpha = 26^\circ$ from the anti-solar direction (Fig. 4.2). This spin axis is forced to precess about the anti-solar direction with a period $T_{\text{prec}} = 10 \text{ hr}$. The telescope boresight is oriented at an angle $\beta = 69^\circ$ away from the spin axis (Fig. 3.1). This β angle is chosen such that $\alpha + \beta > 90^\circ$, enabling mapping of all ecliptic latitudes. The precession axis tracks along with the Earth in its yearly orbit around the Sun, so this scan strategy maps the full sky (all ecliptic longitudes) within 6 months.

PICO’s $\alpha = 26^\circ$ value is chosen to be substantially larger than the *Planck* mission’s α angle (7.5°) to mitigate systematic effects by scanning across each sky pixel with a greater diversity of orientations [99]. Increasing α further would decrease the Sun-shadowed volume available for the optics and consequently reduce the telescope aperture size. A deployable Sunshade was considered, but found not to be required, and was thus excluded in favor of a more conservative and less costly approach.

The instrument spin rate, selected through a trade study, matches that of the *Planck* mission. The

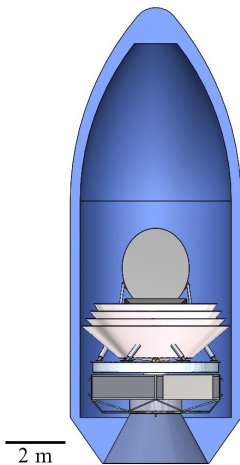


Figure 4.1: PICO is compatible with the Falcon 9.

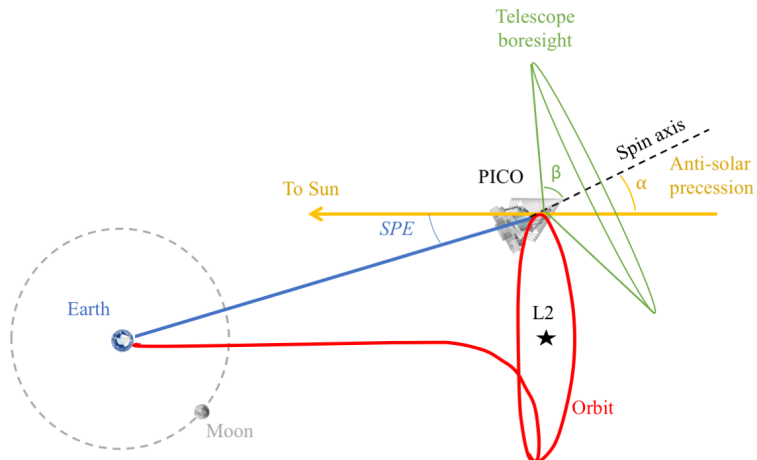


Figure 4.2: PICO surveys by continuously spinning the instrument about a precessing axis.

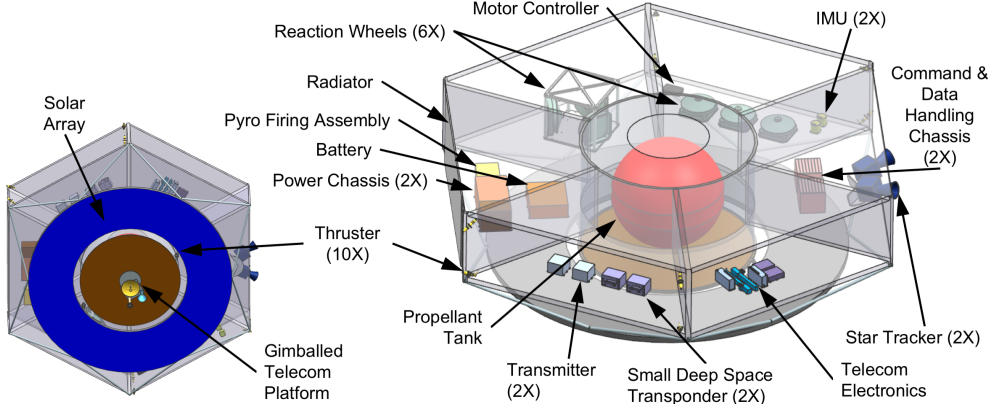


Figure 4.3: Modular equipment bays provide easy access to all components in the spacecraft de-spun module and enable parallel integration of spacecraft subsystems.

study balanced low-frequency ($1/f$) noise subtraction (improves with spin rate) against implementation cost and heritage, pointing reconstruction ability (anti-correlated with spin rate), and data volume (linearly correlated with spin rate). The CMB dipole appears in the PICO data timestream at the spin frequency (1 rpm = 16.7 mHz). Higher multipole signals appear at harmonics of the spin frequency, starting at 33 mHz, above the knee in the detector low-frequency noise (§ 3.2.4). A destriping mapmaker applied in data post-processing effectively operates as a high-pass filter, as demonstrated by *Planck* [100]. PICO’s spin-axis precession frequency is more than 400 times faster than that of *Planck*, greatly reducing the effects of any residual $1/f$ noise by spreading the effects more isotropically across pixels.

4.2 Ground Segment

The PICO Mission Operations System (MOS) and Ground Data System (GDS) can be built with extensive reuse of standard tools. The PICO concept of operations is described in § 4.1. All space-ground communications, ranging, and tracking are performed by the DSN 34 m Beam Wave Guide (BWG). X-band is used to transmit spacecraft commanding, return engineering data, and provide navigation information (S-band is a viable alternative, and could be considered in a future trade). Ka-band is used for high-rate return of science data. The baseline 150 Mb/s transfer rate (130 Mb/s information rate after CCSDS encoding) is an existing DSN catalog service [101]. The instrument produces 6.1 Tb/day, which is compressed to 1.5 Tb/day (§ 3.3). Daily 4 hr DSN passes return PICO data in 3.1 hr, with the remaining 0.9 hr available as needed for retransmission or missed-pass recovery.

4.3 Spacecraft

The PICO spacecraft bus is Class B and designed for a minimum lifetime of 5 years in the L2 environment. Mission-critical elements are redundant. Flight spares, engineering models, and prototypes appropriate to Class B are budgeted.

The aft end of the spacecraft (the “de-spun module”) is comprised of six equipment bays that house standard components (Fig. 4.3). The instrument and V-grooves are mounted on bipods from the spacecraft “spun module,” which contains hosted instrument elements (Fig. 3.1). A motor drives the spun module at 1 rpm to support the science survey requirements (§ 4.1.2). Reaction wheels on the despun module cancel the angular momentum of the spun module and provide three-axis control (§ 4.3.1).

The bipods that mechanically support the instrument are thermally insulating. The passively

radiating V-groove assembly thermally isolates the instrument from solar radiation and from the bus (§ 3.4.3). Like *Planck* [97], the V-grooves are manufactured using honeycomb material. Additional radiators on the spun and despun spacecraft modules ($\sim 1 \text{ m}^2$ each) reject heat dissipated by spacecraft subsystems and hosted instrument elements.

PICO's avionics are dual-string with standard interfaces. Solid-state recorders provide three days of science data storage (4.6 Tbit, § 7.1), enabling retransmission of missed data (§ 4.2).

PICO employs a fully redundant Ka- and X-band telecommunications architecture. The Ka-band system uses a 0.3 m high-gain antenna to support a science data downlink information rate of 130 Mb/s to a 34 m BWG DSN ground station with a link margin of 4.8 dB. The X-band system provides command and engineering telemetry communication through all mission phases using medium- and low-gain antennas. Amplifiers, switches, and all three antennas are on a gimballed platform, enabling Ka and X-band downlink concurrent with science observations.

The heritage power electronics are dual-string. A 74 A-hr Li-ion battery is sized for a 3 hr launch phase with 44 % depth of discharge. After the launch phase, the driving mode is telecom concurrent with science survey (1320 W including 43 % contingency). Solar cells on the aft side of the bus (5.8 m² array, $\alpha = 26^\circ$ off-Sun) support this mode with positive power, and unused area in the solar array plane (7.4 m² more area by growing to 4.5 m diameter) affords 125 % margin (Fig. 4.3).

The propulsion design is a simple mono-propellant blow-down hydrazine system with standard redundancy. Two aft-pointed 22 N thrusters provide ΔV and attitude control for orbit insertion and maintenance (§ 4.1.1), requiring 140 kg of propellant. Eight 4 N thrusters provide reaction-wheel momentum management and backup attitude-control authority (60 kg of propellant). Accounting for ullage (14 kg), the baseline propellant tank fill fraction is 77 %.

4.3.1 Attitude Determination and Control

PICO uses a zero net angular momentum control architecture with heritage from the SMAP mission (§ 7.1). PICO's instrument spin rate (1 rpm) matches that of the *Planck* mission, but the precession of the spin axis is faster (10 hr vs 6 months), and the precession angle larger (26° vs 7.5°). These differences make the spin-stabilized *Planck* control architecture impractical.

The PICO instrument spin rate is achieved and maintained using a spin motor. The spin motor drive electronics provide the coarse spin rate knowledge used for controlling the spin rate to meet the ± 0.1 rpm requirement. Data and power are passed across the interface using slip rings.

PICO requires 220 N m s to cancel the angular momentum of the instrument and spacecraft spun module at 1 RPM. This value includes mass contingency and is based on the CAD model. Three Honeywell HR-16 reaction wheel assemblies (RWAs), each capable of 150 N m s, are mounted on the despun module parallel to the instrument spin axis, and spin opposite to the instrument to achieve zero net angular momentum. The despun module is three-axis stabilized. The spin axis is precessed using three RWAs mounted normal to the spin axis in a triangle configuration. Each set of three RWAs is sized such that two could perform the required function with margin, providing single fault tolerance.

Spin-axis pointing and spin-rate knowledge are achieved and maintained using star tracker and inertial measurement unit (IMU) data. The attitude determination system is single-fault tolerant, with two IMUs each on the spun and despun modules, and two star trackers each on the spun and despun modules. Two Sun sensors on the despun module are used for safe-mode contingencies and instrument Sun avoidance. All attitude control and reconstruction requirements are met, including

spin axis control < 60 arcmin with < 1 arcmin/min stability, and reconstructed pointing knowledge < 10 arcsec (each axis, 3σ).

Additional pointing reconstruction is performed in post-processing using the science data. The PICO instrument will observe planets (compact, bright sources) nearly every day. By fitting the telescope pointing to the known planetary ephemerides, the knowledge of the telescope boresight pointing and the relative pointing of each detector will improve to better than 1 arcsec (each axis, 3σ). *Planck*, with fewer detectors, making lower SNR measurements of the planets, and observing with a scan strategy that acquired measurements of each planet only once every 6 months, demonstrated 0.8 arcsec (1σ) pointing reconstruction uncertainty in-scan and 1.9 arcsec (1σ) cross-scan [102].

5 Technology Drivers

PICO builds off of the heritage of *Planck-HFI* and *Herschel*. Since the time of *Planck* and *Herschel*, suborbital experiments have used monolithically fabricated TES bolometers and multiplexing schemes to field instruments with thousands of TES bolometers per camera (Fig. 5.1). By the time PICO enters Phase A, S3 experiments plan to be operating nearly 100,000

TES bolometers in several independent cameras [104–106].

The remaining technology developments required to enable the PICO baseline design are:

1. extension of three-color antenna-coupled bolometers down to 21 GHz and up to 462 GHz (§ 5.1);
2. construction of high-frequency direct absorbing arrays and laboratory testing (§ 5.2);
3. beam line and 100 mK testing to simulate the cosmic ray environment at L2 (§ 5.3);
4. expansion of time-division multiplexing to support 128 switched rows per readout column (§ 5.4).

All of these developments are straightforward extensions of technologies already available today. We recommend APRA and SAT support to complete development of these technologies through the milestones described in Table 5.1.

5.1 21–462 GHz Bands

Suborbital teams have successfully demonstrated a variety of optical-coupling schemes, including horns with ortho-mode transducers (OMTs), lithographed antenna arrays, and sinuous antennas under lenslets (Table 5.2). All have achieved background-limited performance with sufficient margin on design parameters to achieve this performance in the lower background environment at L2. All have been packaged into modules and focal-plane units in working cameras representative of the PICO integration. Experiments have already used a number of PICO’s observing bands between 27 GHz and 270 GHz (Table 5.2). To date, statistical map depths of $3 \mu\text{K}_{\text{CMB}}$ arcmin have been achieved over small sky areas, which is within a factor of five of PICO’s CBE over the entire sky (Table 3.2).

The baseline PICO instrument requires three-color dual-polarized antenna-coupled bolometers covering bands from 21 to 462 GHz (§ 3.2.1). The sinuous antenna has the bandwidth to service three bands per pixel, whereas horns and antenna arrays have only been used for two. Our baseline is to use a three-band sinuous antenna, although we have designs that use two- or one-band per pixel and have the same or similar baseline noise as PICO (§ 5.5). SPT-3G has used the PICO-baselined three-color pixel design to deploy 16,000 detectors covering 90/150/220 GHz [103].

The extension to lower frequencies requires larger antennas and therefore control of film properties and lithography over larger areas. Scaling to higher frequencies requires tighter fabrication tolerances and electromagnetic wave transmission losses tend to increase due to material properties. Current anti-reflection technologies for the lenslets need to be extended with thicker and thinner layers to cover the lowest and highest frequency channels. These developments will require



Figure 5.1: SPT-3G operates a focal plane with sinuous antenna-coupled, three-band pixels with 16,000 bolometers [103]. Each pixel couples radiation to bands at 95, 150, and 220 GHz.

Table 5.1: PICO technologies can be developed to TRL 5 prior to a 2023 Phase A start using the APRA and SAT programs, requiring a total of about \$ 13M. Per NASA guidance, these costs are outside the mission cost (§ ??).

Task	Current status	Milestone A	Milestone B	Milestone C	Current funding	Required funding	Date TRL5 achieved
1a. Three-color arrays $v < 90 \text{ GHz}$	2-color lab demos $v > 30 \text{ GHz}$	Field demo of 30–40 GHz (2020)	Lab demos 20–90 GHz (2022)	—	APRA & SAT	\$2.5M over 4 yr (1 APRA + 1 SAT)	2022
1b. Three-color arrays $v > 220 \text{ GHz}$	2-color lab demos $v < 300 \text{ GHz}$	Field demo of 150–270 GHz (2021)	Lab demos 150–460 GHz (2022)	—	APRA & SAT	\$3.5M over 4 yr (2 SATs)	2022
2. Direct absorbing arrays $v > 50 \text{ GHz}$	0.1–5 THz unpolarized	Design & prototype of arrays (2021)	Lab demo of 555 GHz (2022)	Lab demo of 799 GHz (2023)	None	\$2M over 5 yr (1 SAT)	2023
3. Cosmic ray studies	250 mK w/ sources	100 mK tests with sources (2021)	Beamline tests (2023)	—	APRA & SAT	\$0.5–1M over 5 yr (part of 1 SAT)	—
4a. Fast readout electronics	MUX66 demo	Engineering and Fab of electronics (2020)	Lab demo (2021)	Field demo (2023)	No direct funds	\$4M over 5 yr (1 SAT)	2023
4b. System engineering; 128× MUX demo	MUX66 demo	Design of cables (2020)	Lab demo (2021)	Field demo (2023)	No direct funds	—	—

Table 5.2: Multiple active suborbital efforts are advancing technologies relevant to PICO.

Project	Type	Optical Coupling	v_c [GHz]	Colors per pixel	N_{bolo}	Significance	Reference
PICO baseline	Flight		21 – 462	Three	11,796		§ 3.2.1
SPT-3G	Ground	Sinuous	90 – 220	Three	16,260	Trichroic	[103]
Advanced ACT-pol .	Ground	Horns	27 – 230	Two	3,072	Dichroic	[107]
BICEP/Keck	Ground	Antenna arrays	90 – 270	One	5,120	50 nK-deg	[108]
Berkeley, Caltech, NIST	Lab	Various	30 – 270	Various	–	Band coverage	[79, 109, 110]
SPIDER	Balloon	Antenna arrays	90 – 150	One	2,400	Stable to 10 mHz	[77]

control of cleanliness and understanding of process parameters. Changes to elements in the light path will require characterization of beam properties.

The direction of polarization sensitivity of the sinuous antenna varies with frequency, thus presenting a potential source of systematic error. Over 25% bandwidth, the variation is approximately $\pm 5 \text{ deg}$ [111]. There are solutions to this in the focal-plane design, measurements, data analysis, and free parameters of the sinuous antenna geometry. A recent study found that pre-flight characterization of the effect through measurements can readily mitigate it as a source of systematic uncertainty [112]. Studies with current field demonstrations, such as with the data of SPT-3G, will be particularly important. The PICO concept is robust to any challenges in developing three-color

Table 5.3: PICO high-frequency detectors leverage development and demonstration by *Planck*, *Herschel*, and SPT.

Project	Type	Polarized	Mono-lithic	v_c [GHz]	Colors per pixel	N_{bolo}	Significance	Reference
PICO baseline	Flight	Yes	Yes	555 – 799	One	1,200		§ 3.2.2
<i>Planck</i> HFI	Flight	143–343 GHz	No	143 – 857	One	48	TRL 9 polarized	[74]
<i>Herschel</i>	Flight	No	Yes	570 – 1200	One	270	TRL 9 monolithic	[114]
SPT-SZ	Ground	No	Yes	90 – 220	One	840	Monolithic array TESs	[72]
SPT-pol-90	Ground	Yes	No	90	One	180	Dual pol absorbing TESs	[115]

pixels; § 5.5 describes options to descope to two- and one-color pixels, technologies for which the polarization sensitivity is constant as a function of frequency.

5.2 555–799 GHz bands

The baseline PICO instrument requires single-color, horn-coupled, dual-polarization, direct-absorbing bolometers from 555 to 799 GHz (§ 3.2.2). *Planck* and *Herschel* demonstrated the architecture of horns coupled to direct absorbing bolometers. Ground experiments with similar designs have deployed focal planes with hundreds of horn-coupled spiderweb bolometers, replacing the *Planck* and *Herschel* NTD-Ge thermistors with TESs, and adjusting time constants as necessary (Table 5.3). *Planck*-HFI, SPT-pol, and BICEP demonstrated dual-polarized detectors. *Herschel* and SPT-SZ demonstrated monolithic unpolarized detectors. PICO will require detectors that merge these two designs in monolithic dual-polarized arrays. Since all the components of the technology already exist, the remaining necessary development is the packaging. Filled arrays of detectors such as Backshort Under Ground (BUG) bolometers are also an option [113].

5.3 Environmental Testing

Laboratory tests and in-flight data from balloons suggest that TES bolometer arrays may be more naturally robust against cosmic rays than the individual NTD-Ge bolometers used in *Planck*. PICO will leverage lessons learned from *Planck* and ensure robust thermal sinking of detector array substrates. Cosmic-ray glitches have fast recovery times and low coincidence rates [116, 117]. Residual risk can be retired with 100 mK testing where the array heat sinking may be weaker, and beam-line tests to simulate the expected flight environment.

5.4 Multiplexing

More than ten experiments have used time-domain multiplexer (TDM) readout. SCUBA2 on JCMT has 10,000 pixels, nearly as many detectors as planned for PICO [118]. Most of these experiments have used 32-row multiplexing. Recently ACT has expanded this to 64-row multiplexing [78].

PICO’s sensitivity requirements dictate the use of 13,000 transition-edge-sensor bolometers and a multiplexed system. Our baseline design is to use TDM readout with 128 switched rows per readout column (TDM-128×). The leap to TDM-128× requires:

- development of fast-switched room temperature electronics; and
- system engineering of room temperature to cryogenic row-select cabling to ensure sufficiently fast row-switch settling times.

The historical row revisit rate for bolometric instruments using 32× TDM has been 25 kHz [e.g.,

[68]. However, X-ray instruments using TDM routinely switch between rows at 6.25 MHz [119]. The PICO baseline assumes a 6.25 MHz switch rate and TDM- $128\times$, which dictates a row-revisit rate of 48.8 kHz. To limit aliased noise, PICO implements low-pass filters in each readout channel with a bandwidth of 6 kHz, dictated by detector stability considerations and the required ~ 1 kHz signal bandwidth. With these parameters and using the same TDM multiplexer SQUID design, the increased total noise due to aliasing is less than 15 % and is included in our detector noise budget. The system engineering study will culminate in a demonstration of TDM- $128\times$ SQUID aliased noise below PICO detector sensitivity requirements.

5.5 Technology Descores

A descope from three-color sinuous antenna/lenslet-coupled pixels to two-color horn-coupled, or to single color antenna-array pixels remains a viable alternative should the three-color technology not mature as planned. In both alternative options, bands above 555 GHz are the same as the baseline. For the lower frequencies, the two-color horn-coupled pixel option contains 8,840 detectors and has 19 colors. Because horns have a 2.3 : 1 bandwidth, each of the two bands in a pixel has 35 % bandwidth (compared to the baseline 25 %), which compensates for pixel count, resulting in $0.61 \mu\text{K}_{\text{CMB}}$ arcmin aggregate CBE map depth. This is the same as the three-color CBE map depth, and affords the same 40 % margin relative to the $0.87 \mu\text{K}_{\text{CMB}}$ arcmin baseline requirement (Table 3.2). Detailed analysis would be performed to assess the impact of the coarser spectral resolution on signal component separation. Single color antenna-array pixels can have higher packing density than the other two architectures. This option has 6,540 detectors, 21 colors, each with 30 % bandwidth, and a noise level of $0.74 \mu\text{K}_{\text{CMB}}$ arcmin, leaving only 17% noise margin relative to the requirement.

5.6 Enhancing Technologies

The following technologies are neither required nor assumed by the PICO baseline concept. However, they represent opportunities to extend scientific capabilities or simplify engineering.

PICO baselines TDM readout because of its relative maturity and demonstrated sensitivity and stability in relevant science missions. Lab tests of frequency-domain multiplexing (FDM) give comparable performance with higher multiplexing factors and lower thermal loads on cryogenic stages relative to TDM, but with higher ambient temperature power consumption. Suborbital experiments such as SPT-3G are using FDM to read out focal planes comparable in size to PICO.

Microwave frequency SQUID multiplexing can increase the multiplexing density and reduce the number of wires between the 4 K and ambient temperature stages [120, 121]. Kinetic inductance detectors and Thermal KIDs can further reduce the wire count, obviate the need for SQUID-based amplifiers, and simplify integration by integrating the multiplexing function on the same substrate as the detectors [122–124]. The cost to develop these technologies is \$3–4M/year, with a high chance of reaching TRL-5 before Phase A.

6 Organization, Partnerships, and Current Status

PICO is the result of an 18-months mission study funded by NASA (total grant = \$150,000). The study was open to the entire mm/sub-mm community. Seven working groups were led by members of PICO’s Executive Committee, which had a telephone conference weekly, led by the PI. A three-member steering committee, composed of two experimentalists experienced with CMB space missions, and a senior theorist gave occasional advice to the PI. More than 60 scientists, international-

and US-based, participated in-person in each of two community workshops (November 2017 and May 2018). The study report has been submitted by NASA to the decadal panel, and it is available on the arXiv and on the PICO website [58, 125]. It has contributions from 82 authors, and has been endorsed by additional 131 members of the community.

The PICO team designed an entirely US-based mission, so that the full cost of the mission can be assessed. We excluded contributions by other space agencies, despite expression of interest by international scientists. The PICO concept has wide support in the international community. If the mission is selected to proceed, a path that would be scientifically and financially optimal relative to other options, it is reasonable to expect that international partners would participate and thus reduce the US cost of the mission.

7 Schedule and Cost

	FY24	FY25	FY26	FY27	FY28	FY29	FY30	FY31	FY32	FY33	FY34	FY35
CY 2023	CY 2024	CY 2025	CY 2026	CY 2027	CY 2028	CY 2029	CY 30	CY 31	CY 32	CY 33	CY 34	
PH A (12 mths)	PH B (12 mths)	PHASE C (22 mths)	PHASE D(18 mths)		PHASE E (5 yrs)							F 4 mths
♦ 10/23 KDP-A	♦ 10/24 KDP-B	♦10/25 KDP-C		♦ 8/27 KDP-D		♦ 2/29 PLAR (Start of Ph E)						KDP-F 2/34 ♦
Reviews	10/25 PDR ♦		♦ 7/26 CDR	♦ 7/27 ARR		Launch 1/29★						

Figure 7.1: PICO development and operations schedule.

- Schedule** NASA-funded Probe studies including PICO assume a Phase A start in October 2023. PICO development phases B-D are similar in duration to recent comparably sized NASA missions such as Juno and SMAP. PICO is a cryogenic mission similar to *Planck*, but the cryogenic design is simpler because all PICO’s bolometric detectors are maintained at 0.1 K (*Planck*’s bolometers were maintained at 0.1 K, and the radiometers at 20 K). We used experience from *Planck* and from current implementations of ground-based kilo-pixel arrays to allocate appropriate time for integration and testing (I&T).

The baseline mission lifetime is 5 years. The PICO instrument does not have cryogenic consumables (as *Planck* did), permitting mission extension beyond the prime mission duration.

- Cost** We estimate PICO’s total Phase A–E lifecycle cost between \$870M and \$960M, including the \$150M allocation for the Launch Vehicle (per NASA direction). These cost estimates include 30 % reserves for development (Phases A–D) and 13 % reserves for operations (Phase E). Table 7.1 shows the JPL Team X

Table 7.1: Detailed breakdown of Team X and PICO Team cost estimates (in FY18\$). Costs are based on the schedule in Fig. 7.1, which includes 5 years of operations.

Work Breakdown Structure (WBS) elements	Team X	PICO
Development Cost (Phases A–D)	\$ 724M	\$ 634–677M
1.0, 2.0, 3.0 Management, Systems Engineering, and Mission Assurance	\$ 54M	\$ 47– 50M
4.0 Science		\$ 19M
5.0 Payload System		\$ 168M
6.0 Flight System	\$ 248M	\$ 210–240M
10.0 Assembly, Test, and Launch Operations (ATLO)	\$ 24M	
7.0 Mission Operations Preparation		\$ 16M
9.0 Ground Data Systems		\$ 21M
12.0 Mission and Navigation Design		\$ 7M
Development Reserves (30%)	\$167M	\$ 146–156M
Operations Cost (Phase E)		\$ 84M
1.0 Management		\$ 6M
4.0 Science		\$ 20M
7.0 Mission Operations		\$ 34M
9.0 Ground Data Systems		\$ 14M
Operations Reserves (13%)		\$ 10M
Launch Vehicle Cost		\$ 150M
Total Cost	\$ 958M	\$ 868–911M

and the PICO team mission cost breakdown.

Team X estimates are generally model-based, and were generated after a series of instrument and mission-level studies. The PICO team adopted the Team X estimates, but also obtained a parametrically estimated cost range for the Flight System and Assembly, Test, and Launch Operations from Lockheed Martin Corporation to represent the cost benefits that might be realized by working with an industry partner. After adding estimated JPL overhead the PICO team cost is in-family with but lower than the Team X cost.

Science team costs are assessed by Team X based on PICO science team estimates of the numbers and types of contributors and meetings required for each year of PICO mission development and operations. These workforce estimates are informed by recent experience with the *Planck* mission. PICO’s spacecraft cost reflects a robust Class B architecture. Mission-critical elements are redundant. Appropriate flight spares, engineering models and prototypes are included. Mission operations, Ground Data Systems, and Mission Navigation and Design costs reflect the relatively simple operations: PICO has a single instrument and a single, repetitive science observing mode.

The active cooling system (the 0.1 K cADR and 4 K cryocooler) comprises nearly half of the payload cost. The cADR cost for this study is an estimate from Goddard Space Flight Center. The 4 K cryocooler cost for this study is based on the NASA Instrument Cost Model (NICM) VIII CER Cryocooler model [126], assuming a commercial build. Based on JPL experience, 18 % of the instrument cost is allocated for integration and testing (I&T). More details on the cost of PICO are available in the full PICO report [58].

7.1 Heritage

PICO’s reflectors are similar to *Planck*’s, but somewhat larger (270 cm × 205 cm primary versus 189 cm × 155 cm) [127]. *Herschel* observed at shorter wavelengths that required higher surface accuracy and had a larger reflector (350 cm diameter primary) [128]. PICO’s detectors are cooled by a cADR with requirements that are within the capabilities of current ADRs developed by Goddard Space Flight Center. These systems have been applied to several JAXA missions, including *Hitomi* [91]. PICO’s 4 K cryocooler (§ 3.4.2) is a direct extension of the JWST MIRI design [92, 93]. PICO benefits from a simpler and more reliable implementation of the J-T system than was required for MIRI, in that no deployment of cooling lines is required, and all flow valving is performed on the warm spacecraft. Structures similar to PICO’s V-groove radiator assembly are a standard approach for passive cooling, and were first described more than thirty years ago [129]. PICO’s spin system is less demanding than the successful SMAP spin system. The PICO spin rate is 1 rpm, and the mission requires ∼ 220 N m s of spin angular momentum cancellation. The PICO’s data volume and downlink rates are already surpassed by missions in development.

References

- [1] National Research Council, *New Worlds, New Horizons in Astronomy and Astrophysics*. Washington, DC: The National Academies Press, 2010. <https://www.nap.edu/catalog/12951/new-worlds-new-horizons-in-astronomy-and-astrophysics>
- [2] S. Shandera, P. Adshead, M. Amin *et al.*, “Probing the origin of our Universe through cosmic microwave background constraints on gravitational waves,” in *Bulletin of the American Astronomical Society*, ser. *Bull. Am. Astron. Soc.*, vol. 51, May 2019, p. 338. <https://ui.adsabs.harvard.edu/abs/2019BAAS...51c.338S>
- [3] T. R. Slatyer, N. Padmanabhan, and D. P. Finkbeiner, “Cmb constraints on wimp annihilation: Energy absorption during the recombination epoch,” *Physical Review D (Particles, Fields, Gravitation, and Cosmology)*, vol. 80, no. 4, p. 043526, 2009. <http://link.aps.org/abstract/PRD/v80/e043526>
- [4] S. Galli, F. Iocco, G. Bertone, and A. Melchiorri, “CMB constraints on dark matter models with large annihilation cross section,” *Phys. Rev. D.*, vol. 80, no. 2, pp. 023505–+, Jul. 2009. <http://adsabs.harvard.edu/abs/2009PhRvD..80b3505G>
- [5] G. Hütsi, A. Hektor, and M. Raidal, “Constraints on leptionically annihilating dark matter from reionization and extragalactic gamma background,” *Astron. Astrophys.*, vol. 505, pp. 999–1005, Oct. 2009. <http://adsabs.harvard.edu/abs/2009A%26A...505..999H>
- [6] G. Hütsi, J. Chluba, A. Hektor, and M. Raidal, “WMAP7 and future CMB constraints on annihilating dark matter: implications for GeV-scale WIMPs,” *Astron. Astrophys.*, vol. 535, p. A26, Nov. 2011. <http://adsabs.harvard.edu/abs/2011A%26A...535A..26H>
- [7] M. S. Madhavacheril, N. Sehgal, and T. R. Slatyer, “Current dark matter annihilation constraints from CMB and low-redshift data,” *Phys. Rev. D.*, vol. 89, no. 10, p. 103508, May 2014. <http://adsabs.harvard.edu/abs/2014PhRvD..89j3508M>
- [8] D. Green, P. D. Meerburg, and J. Meyers, “Aspects of Dark Matter Annihilation in Cosmology,” *ArXiv e-prints*, Apr. 2018. <http://adsabs.harvard.edu/abs/2018arXiv180401055G>
- [9] L. M. Widrow, “Origin of galactic and extragalactic magnetic fields,” *Reviews of Modern Physics*, vol. 74, pp. 775–823, 2002. <http://adsabs.harvard.edu/abs/2002RvMP...74..775W>
- [10] L. M. Widrow, D. Ryu, D. R. G. Schleicher, K. Subramanian, C. G. Tsagas, and R. A. Treumann, “The First Magnetic Fields,” *Space Science Reviews*, vol. 166, pp. 37–70, May 2012. <http://adsabs.harvard.edu/abs/2012SSRv..166..37W>
- [11] R. M. Athreya, V. K. Kapahi, P. J. McCarthy, and W. van Breugel, “Large rotation measures in radio galaxies at $Z > 2$,” *Astron. Astrophys.*, vol. 329, pp. 809–820, Jan. 1998. <http://adsabs.harvard.edu/abs/1998A%26A...329..809A>
- [12] D. Grasso and H. R. Rubinstein, “Magnetic fields in the early Universe,” *Physics Reports*, vol. 348, pp. 163–266, Jul. 2001. <http://adsabs.harvard.edu/abs/2001PhR...348..163G>
- [13] T. Vachaspati, “Magnetic fields from cosmological phase transitions,” *Physics Letters B*, vol. 265, pp. 258–261, Aug. 1991. <http://adsabs.harvard.edu/abs/1991PhLB..265..258V>
- [14] M. S. Turner and L. M. Widrow, “Inflation-produced, large-scale magnetic fields,” *Phys. Rev. D.*, vol. 37, pp. 2743–2754, May 1988. <http://adsabs.harvard.edu/abs/1988PhRvD..37.2743T>
- [15] B. Ratra, “Cosmological ‘seed’ magnetic field from inflation,” *Ap. J. Lett.*, vol. 391, pp. L1–L4, May 1992. <http://adsabs.harvard.edu/abs/1992ApJ...391L...1R>
- [16] A. Díaz-Gil, J. García-Bellido, M. García Pérez, and A. González-Arroyo, “Magnetic Field Production during Preheating at the Electroweak Scale,” *Physical Review Letters*, vol. 100, no. 24, p. 241301, Jun. 2008. <http://adsabs.harvard.edu/abs/2008PhRvL..100x1301D>
- [17] N. Barnaby, R. Namba, and M. Peloso, “Observable non-Gaussianity from gauge field production in slow roll inflation, and a challenging connection with magnetogenesis,” *Phys. Rev. D.*, vol. 85, no. 12, p. 123523, Jun. 2012. <http://adsabs.harvard.edu/abs/2012PhRvD..85l3523B>
- [18] A. J. Long, E. Sabancilar, and T. Vachaspati, “Leptogenesis and primordial magnetic fields,” *JCAP*, vol. 2, p. 036, Feb. 2014. <http://adsabs.harvard.edu/abs/2014JCAP..02..036L>
- [19] R. Durrer and A. Neronov, “Cosmological magnetic fields: their generation, evolution and observation,” *Astronomy and Astrophysics Review*, vol. 21, p. 62, Jun. 2013. <http://adsabs.harvard.edu/abs/2013A%26ARv..21...62D>

- [20] N. Oppermann, H. Junklewitz, G. Robbers *et al.*, “An improved map of the Galactic Faraday sky,” *Astron. Astrophys.*, vol. 542, p. A93, Jun. 2012. <http://adsabs.harvard.edu/abs/2012AA..542A..93O>
- [21] S. De, L. Pogosian, and T. Vachaspati, “CMB Faraday rotation as seen through the Milky Way,” *Phys. Rev. D.*, vol. 88, no. 6, p. 063527, Sep. 2013. <http://adsabs.harvard.edu/abs/2013PhRvD..88f3527D>
- [22] L. Pogosian, “Searching for primordial magnetism with multifrequency cosmic microwave background experiments,” *MNRAS*, vol. 438, pp. 2508–2512, Mar. 2014. <http://adsabs.harvard.edu/abs/2014MNRAS.438.2508P>
- [23] K. Freese, J. A. Frieman, and A. V. Olinto, “Natural inflation with pseudo Nambu-Goldstone bosons,” *Physical Review Letters*, vol. 65, pp. 3233–3236, Dec. 1990. <http://adsabs.harvard.edu/abs/1990PhRvL..65.3233F>
- [24] J. A. Frieman, C. T. Hill, A. Stebbins, and I. Waga, “Cosmology with Ultralight Pseudo Nambu-Goldstone Bosons,” *Physical Review Letters*, vol. 75, pp. 2077–2080, Sep. 1995. <http://adsabs.harvard.edu/abs/1995PhRvL..75.2077F>
- [25] S. M. Carroll, “Quintessence and the Rest of the World: Suppressing Long-Range Interactions,” *Physical Review Letters*, vol. 81, pp. 3067–3070, Oct. 1998. <http://adsabs.harvard.edu/abs/1998PhRvL..81.3067C>
- [26] N. Kaloper and L. Sorbo, “Of pNGB quiScript Ntessence,” *JCAP*, vol. 4, p. 007, Apr. 2006. <http://adsabs.harvard.edu/abs/2006JCAP..04..007K>
- [27] C. R. Contaldi, J. Magueijo, and L. Smolin, “Anomalous Cosmic-Microwave-Background Polarization and Gravitational Chirality,” *Phys. Rev. Lett.*, vol. 101, p. 141101, Oct. 2008. <https://ui.adsabs.harvard.edu/#abs/2008PhRvL.101n1101C>
- [28] V. Gluscevic and M. Kamionkowski, “Testing parity-violating mechanisms with cosmic microwave background experiments,” *Phys. Rev. D.*, vol. 81, no. 12, p. 123529, Jun. 2010. <http://adsabs.harvard.edu/abs/2010PhRvD..81l3529G>
- [29] D. Harari and P. Sikivie, “Effects of a Nambu-Goldstone boson on the polarization of radio galaxies and the cosmic microwave background,” *Physics Letters B*, vol. 289, pp. 67–72, Sep. 1992. <http://adsabs.harvard.edu/abs/1992PhLB..289..67H>
- [30] S. M. Carroll, G. B. Field, and R. Jackiw, “Limits on a Lorentz- and parity-violating modification of electrodynamics,” *Phys. Rev. D.*, vol. 41, pp. 1231–1240, Feb. 1990. <http://adsabs.harvard.edu/abs/1990PhRvD..41.1231C>
- [31] M. Kamionkowski, “How to Derotate the Cosmic Microwave Background Polarization,” *Physical Review Letters*, vol. 102, no. 11, p. 111302, Mar. 2009. <http://adsabs.harvard.edu/abs/2009PhRvL.102k1302K>
- [32] V. Gluscevic, M. Kamionkowski, and A. Cooray, “Derotation of the cosmic microwave background polarization: Full-sky formalism,” *Phys. Rev. D.*, vol. 80, no. 2, p. 023510, Jul. 2009. <http://adsabs.harvard.edu/abs/2009PhRvD..80b3510G>
- [33] V. Gluscevic, D. Hanson, M. Kamionkowski, and C. M. Hirata, “First CMB constraints on direction-dependent cosmological birefringence from WMAP-7,” *Phys. Rev. D.*, vol. 86, no. 10, p. 103529, Nov. 2012. <http://adsabs.harvard.edu/abs/2012PhRvD..86j3529G>
- [34] P. Svrcek and E. Witten, “Axions in string theory,” *Journal of High Energy Physics*, vol. 6, p. 051, Jun. 2006. <http://adsabs.harvard.edu/abs/2006JHEP..06..051S>
- [35] M. Pospelov, A. Ritz, and C. Skordis, “Pseudoscalar Perturbations and Polarization of the Cosmic Microwave Background,” *Physical Review Letters*, vol. 103, no. 5, p. 051302, Jul. 2009. <http://adsabs.harvard.edu/abs/2009PhRvL.103e1302P>
- [36] V. Miranda, A. Lidz, C. H. Heinrich, and W. Hu, “CMB signatures of metal-free star formation and Planck 2015 polarization data,” *MNRAS*, vol. 467, pp. 4050–4056, Jun. 2017. <http://adsabs.harvard.edu/abs/2017MNRAS.467.4050M>
- [37] LSST Science Collaboration, P. A. Abell, J. Allison *et al.*, “LSST Science Book, Version 2.0,” *arXiv e-prints*, Dec. 2009. <http://adsabs.harvard.edu/abs/2009arXiv0912.0201L>
- [38] J. S. Dunlop, “Observing the First Galaxies,” in *The First Galaxies*, ser. Astrophysics and Space Science Library, T. Wiklind, B. Mobasher, and V. Bromm, Eds., vol. 396, 2013, p. 223. <http://adsabs.harvard.edu/abs/2013ASSL..396..223D>
- [39] M. Schmittfull and U. Seljak, “Parameter constraints from cross-correlation of CMB lensing with galaxy clustering,” *Phys. Rev. D.*, vol. 97, no. 12, p. 123540, Jun. 2018. <http://adsabs.harvard.edu/abs/2018PhRvD..97l3540S>

- [40] Y. Ono, M. Ouchi, Y. Harikane *et al.*, “Great Optically Luminous Dropout Research Using Subaru HSC (GOLDRUSH). I. UV luminosity functions at $z = 4$ -7 derived with the half-million dropouts on the 100 deg² sky,” *Publications of the Astronomical Society of Japan*, vol. 70, p. S10, Jan. 2018. <http://adsabs.harvard.edu/abs/2018PASJ...70S..10O>
- [41] Y. Harikane, M. Ouchi, Y. Ono *et al.*, “GOLDRUSH. II. Clustering of galaxies at $z = 4$ -6 revealed with the half-million dropouts over the 100 deg² area corresponding to 1 Gpc³,” *Publications of the Astronomical Society of Japan*, vol. 70, p. S11, Jan. 2018. <http://adsabs.harvard.edu/abs/2018PASJ...70S..11H>
- [42] J.-B. Melin, J. G. Bartlett, Z.-Y. Cai, G. De Zotti, J. Delabrouille, M. Roman, and A. Bonaldi, “Dust in galaxy clusters: Modeling at millimeter wavelengths and impact on Planck cluster cosmology,” *Astron. Astrophys.*, vol. 617, p. A75, Sep. 2018.
- [43] Y. B. Zeldovich and R. A. Sunyaev, “The Interaction of Matter and Radiation in a Hot-Model Universe,” *ApSS*, vol. 4, pp. 301–316, Jul. 1969. <http://adsabs.harvard.edu/abs/1969Ap%26SS...4..301Z>
- [44] R. A. Sunyaev and Y. B. Zeldovich, “The Observations of Relic Radiation as a Test of the Nature of X-Ray Radiation from the Clusters of Galaxies,” *Comments on Astrophysics and Space Physics*, vol. 4, p. 173, Nov. 1972. <http://adsabs.harvard.edu/abs/1972CoASP..4..173S>
- [45] E. Di Valentino, T. Brinckmann, M. Gerbino *et al.*, “Exploring cosmic origins with CORE: Cosmological parameters,” *JCAP*, vol. 4, p. 017, Apr. 2018. <http://adsabs.harvard.edu/abs/2018JCAP...04..017D>
- [46] Y. Wang, “Figure of merit for dark energy constraints from current observational data,” *Phys. Rev. D.*, vol. 77, no. 12, p. 123525, Jun. 2008. <http://adsabs.harvard.edu/abs/2008PhRvD..77I3525W>
- [47] M. Tanabashi, K. Hagiwara, K. Hikasa *et al.*, “Review of Particle Physics*,” *Phys. Rev. D.*, vol. 98, no. 3, p. 030001, Aug. 2018. <http://adsabs.harvard.edu/abs/2018PhRvD..98c0001T>
- [48] T. Namikawa, S. Saito, and A. Taruya, “Probing dark energy and neutrino mass from upcoming lensing experiments of CMB and galaxies,” *JCAP*, vol. 12, p. 027, Dec. 2010. <http://adsabs.harvard.edu/abs/2010JCAP...12..027N>
- [49] PICO website, “Testing Λ CDM.” <https://sites.google.com/umn.edu/picomission/home/testlcdm>
- [50] Planck Collaboration, N. Aghanim, Y. Akrami *et al.*, “Planck 2018 results. XII. Galactic astrophysics using polarized dust emission,” *ArXiv e-prints*, Jul. 2018. <https://ui.adsabs.harvard.edu/#abs/2018arXiv180706212P>
- [51] D. T. Chuss, B.-G. Andersson, J. Bally *et al.*, “HAWC+/SOFIA Multiwavelength Polarimetric Observations of OMC-1,” *ArXiv e-prints*, Oct. 2018. <https://ui.adsabs.harvard.edu/#abs/2018arXiv181008233C>
- [52] F. Bacciotti, J. M. Girart, M. Padovani *et al.*, “ALMA Observations of Polarized Emission toward the CW Tau and DG Tau Protoplanetary Disks: Constraints on Dust Grain Growth and Settling,” *Ap. J.*, vol. 865, p. L12, Oct. 2018. <https://ui.adsabs.harvard.edu/#abs/2018ApJ...865L..12B>
- [53] A. M. Meisner and D. P. Finkbeiner, “Modeling Thermal Dust Emission with Two Components: Application to the Planck High Frequency Instrument Maps,” *Ap. J.*, vol. 798, p. 88, Jan. 2015. <https://ui.adsabs.harvard.edu/#abs/2015ApJ...798..88M>
- [54] B. T. Draine and A. A. Fraisse, “Polarized Far-Infrared and Submillimeter Emission from Interstellar Dust,” *Ap. J.*, vol. 696, pp. 1–11, May 2009. <http://adsabs.harvard.edu/abs/2009ApJ...696....1D>
- [55] V. Guillet, L. Fanciullo, L. Verstraete *et al.*, “Dust models compatible with Planck intensity and polarization data in translucent lines of sight,” *Astron. Astrophys.*, vol. 610, p. A16, Feb. 2018. <http://adsabs.harvard.edu/abs/2018A%26A...610A..16G>
- [56] B. T. Draine and B. Hensley, “Magnetic Nanoparticles in the Interstellar Medium: Emission Spectrum and Polarization,” *Ap. J.*, vol. 765, p. 159, Mar. 2013. <http://adsabs.harvard.edu/abs/2013ApJ...765..159D>
- [57] Planck Collaboration, R. Adam, P. A. R. Ade *et al.*, “Planck intermediate results. XXX. The angular power spectrum of polarized dust emission at intermediate and high Galactic latitudes,” *Astron. Astrophys.*, vol. 586, p. A133, Feb. 2016. <http://adsabs.harvard.edu/abs/2016A%26A...586A.133P>
- [58] S. Hanany, M. Alvarez, E. Artis *et al.*, “PICO: Probe of Inflation and Cosmic Origins,” *arXiv e-prints*, Feb. 2019. <https://ui.adsabs.harvard.edu/abs/2019arXiv190210541H>
- [59] H. K. Eriksen, J. B. Jewell, C. Dickinson, A. J. Banday, K. M. Górski, and C. R. Lawrence, “Joint Bayesian Component Separation and CMB Power Spectrum Estimation,” *Ap. J.*, vol. 676, pp. 10–32, Mar. 2008. <http://adsabs.harvard.edu/abs/2008ApJ...676...10E>
- [60] PICO website, “Simulating dipole calibration for PICO.” https://sites.google.com/umn.edu/picomission/home/simulating_dipole_pico

- [61] J. H. Kang, P. A. R. Ade, Z. Ahmed *et al.*, “2017 upgrade and performance of BICEP3: a 95GHz refracting telescope for degree-scale CMB polarization,” in *Millimeter, Submillimeter, and Far-Infrared Detectors and Instrumentation for Astronomy IX*, ser. Society of Photo-Optical Instrumentation Engineers (SPIE) Conference Series, vol. 10708, Jul. 2018, p. 107082N. <http://adsabs.harvard.edu/abs/2018SPIE10708E..2NK>
- [62] Private communication.
- [63] K. Young, M. Alvarez, N. Battaglia *et al.*, “Optical design of PICO: a concept for a space mission to probe inflation and cosmic origins,” in *Society of Photo-Optical Instrumentation Engineers (SPIE) Conference Series*, vol. 10698, Aug. 2018, p. 1069846. <https://ui.adsabs.harvard.edu/#abs/2018SPIE10698E..46Y>
- [64] P. de Bernardis, P. A. R. Ade, J. J. A. Baselmans *et al.*, “Exploring cosmic origins with CORE: The instrument,” *Journal of Cosmology and Astro-Particle Physics*, vol. 2018, p. 015, Apr. 2018. <https://ui.adsabs.harvard.edu/#abs/2018JCAP..04..015D>
- [65] C. Dragone, “Offset Multireflector Antennas with Perfect Pattern Symmetry and Polarization Discrimination,” *Bell Syst. Tech. J.*, vol. 57, pp. 2663–2684, 178. <http://adsabs.harvard.edu/abs/1978ATTTJ..57.2663D>
- [66] C. Granet, “Designing classical Dragonian offset dual-reflector antennas from combinations of prescribed geometric parameters,” *IEEE Antennas and Propagation Magazine*, vol. 43, pp. 100–107, Dec. 2001. <https://ui.adsabs.harvard.edu/#abs/2001IAPM..43..100G>
- [67] S. M. Duff, J. Austermann, J. A. Beall *et al.*, “Advanced ACTPol Multichroic Polarimeter Array Fabrication Process for 150 mm Wafers,” *Journal of Low Temperature Physics*, vol. 184, pp. 634–641, Aug. 2016. <https://ui.adsabs.harvard.edu/#abs/2016JLTP..184..634D>
- [68] BICEP2 Collaboration, Keck Array Collaboration, SPIDER Collaboration *et al.*, “Antenna-coupled TES Bolometers Used in BICEP2, Keck Array, and Spider,” *Ap. J.*, vol. 812, p. 176, Oct. 2015. <https://ui.adsabs.harvard.edu/#abs/2015ApJ..812..176B>
- [69] J. M. Edwards, R. O’Brient, A. T. Lee, and G. M. Rebeiz, “Dual-Polarized Sinuous Antennas on Extended Hemispherical Silicon Lenses,” *IEEE Transactions on Antennas and Propagation*, vol. 60, pp. 4082–4091, Sep. 2012. <https://ui.adsabs.harvard.edu/#abs/2012ITAP..60.4082E>
- [70] A. Suzuki, K. Arnold, J. Edwards *et al.*, “Multi-Chroic Dual-Polarization Bolometric Detectors for Studies of the Cosmic Microwave Background,” *Journal of Low Temperature Physics*, vol. 176, pp. 650–656, Sep. 2014. <https://ui.adsabs.harvard.edu/#abs/2014JLTP..176..650S>
- [71] R. O’Brient, P. Ade, K. Arnold *et al.*, “A dual-polarized broadband planar antenna and channelizing filter bank for millimeter wavelengths,” *Applied Physics Letters*, vol. 102, p. 063506, Feb. 2013. <https://ui.adsabs.harvard.edu/#abs/2013ApPhL.102f3506O>
- [72] E. D. Shirokoff, “The South Pole Telescope bolometer array and the measurement of secondary Cosmic Microwave Background anisotropy at small angular scales,” Ph.D. dissertation, University of California, Berkeley, Jan. 2011. <https://ui.adsabs.harvard.edu/#abs/2011PhDT.....383S>
- [73] L. Bleem, P. Ade, K. Aird *et al.*, “An Overview of the SPTpol Experiment,” *Journal of Low Temperature Physics*, vol. 167, pp. 859–864, Jun. 2012. <https://ui.adsabs.harvard.edu/#abs/2012JLTP..167..859B>
- [74] A. D. Turner, J. J. Bock, J. W. Beeman *et al.*, “Silicon nitride Micromesh Bolometer Array for Submillimeter Astrophysics,” *Appl. Optics*, vol. 40, pp. 4921–4932, Oct. 2001. <https://ui.adsabs.harvard.edu/#abs/2001ApOpt..40.4921T>
- [75] PICO website, “Q/U Pixel Layout for PICO.” https://sites.google.com/umn.edu/picomission/home/qu_pixels
- [76] A. D. Beyer, M. E. Kenyon, P. M. Echternach *et al.*, “Ultra-sensitive Transition-Edge Sensors for the Background Limited Infrared/Sub-mm Spectrograph (BLISS),” *Journal of Low Temperature Physics*, vol. 167, pp. 182–187, May 2012. <http://adsabs.harvard.edu/abs/2012JLTP..167..182B>
- [77] A. S. Rahlin, P. A. R. Ade, M. Amiri *et al.*, “Pre-flight integration and characterization of the SPIDER balloon-borne telescope,” in *Millimeter, Submillimeter, and Far-Infrared Detectors and Instrumentation for Astronomy VII*, vol. 9153, Jul. 2014, p. 915313. <https://ui.adsabs.harvard.edu/#abs/2014SPIE.9153E..13R>
- [78] S. W. Henderson, R. Allison, J. Austermann *et al.*, “Advanced ACTPol Cryogenic Detector Arrays and Readout,” *Journal of Low Temperature Physics*, vol. 184, pp. 772–779, Aug. 2016. <https://ui.adsabs.harvard.edu/#abs/2016JLTP..184..772H>
- [79] H. Hui, P. A. R. Ade, Z. Ahmed *et al.*, “BICEP Array: a multi-frequency degree-scale CMB polarimeter,” in *Society of Photo-Optical Instrumentation Engineers (SPIE) Conference Series*, vol. 10708, Jul. 2018, p. 1070807. <https://ui.adsabs.harvard.edu/#abs/2018SPIE10708E..07H>

- [80] M. C. Runyan, P. A. R. Ade, M. Amiri *et al.*, “Design and performance of the SPIDER instrument,” in *Millimeter, Submillimeter, and Far-Infrared Detectors and Instrumentation for Astronomy V*, vol. 7741, Jul. 2010, p. 77411O. <https://ui.adsabs.harvard.edu/#abs/2010SPIE.7741E..1OR>
- [81] Z. D. Kermish, “The POLARBEAR Experiment: Design and Characterization,” Ph.D. dissertation, University of California, Berkeley, 2012. <http://adsabs.harvard.edu/abs/2012PhDT.....145K>
- [82] EBEX Collaboration, A. M. Aboobaker, P. Ade *et al.*, “The EBEX Balloon-borne Experiment: Optics, Receiver, and Polarimetry,” *The Astrophysical Journal Supplement Series*, vol. 239, p. 7, Nov. 2018. <https://ui.adsabs.harvard.edu/#abs/2018ApJS..239....7T>
- [83] BICEP2 Collaboration, P. A. R. Ade, R. W. Aikin *et al.*, “Detection of B-Mode Polarization at Degree Angular Scales by BICEP2,” *Phys. Rev. Lett.*, vol. 112, p. 241101, Jun. 2014. <https://ui.adsabs.harvard.edu/#abs/2014PhRvL.112x1101B>
- [84] F. Pajot, “Planck compression,” Private communication.
- [85] Planck HFI Core Team, P. A. R. Ade, N. Aghanim *et al.*, “Planck early results. IV. First assessment of the High Frequency Instrument in-flight performance,” *Astron. Astrophys.*, vol. 536, p. A4, Dec. 2011. <https://ui.adsabs.harvard.edu/#abs/2011A&A...536A...4P>
- [86] The EBEX Collaboration, A. Aboobaker, P. Ade *et al.*, “The EBEX Balloon-borne Experiment—Gondola, Attitude Control, and Control Software,” *The Astrophysical Journal Supplement Series*, vol. 239, p. 9, Nov. 2018. <https://ui.adsabs.harvard.edu/#abs/2018ApJS..239....9T>
- [87] M. Donabedian, A. I. of Aeronautics, and Astronautics, *Spacecraft Thermal Control Handbook, Vol. 2: Cryogenics*, ser. EngineeringPro collection. Aerospace Press, 2003. <https://books.google.com/books?id=nsLqjwEACAAJ>
- [88] R. G. Ross, “Estimation of thermal conduction loads for structural supports of cryogenic spacecraft assemblies,” *Cryogenics*, vol. 44, pp. 421–424, Jun. 2004. <https://ui.adsabs.harvard.edu/#abs/2004Cryo...44..421R>
- [89] M. Petach and M. Michaelian, “Mid InfraRed Instrument (MIRI) cooler cold head assembly acceptance testing and characterization,” *Cryocoolers*, vol. 18, p. 11, 2014. <https://cryocoolerorg.wildapricot.org/resources/Documents/C18/002.pdf>
- [90] P. J. Shirron, M. O. Kimball, D. J. Fixsen, A. J. Kogut, X. Li, and M. J. DiPirro, “Design of the PIXIE adiabatic demagnetization refrigerators,” *Cryogenics*, vol. 52, pp. 140–144, Apr. 2012. <https://ui.adsabs.harvard.edu/#abs/2012Cryo...52..140S>
- [91] P. J. Shirron, M. O. Kimball, B. L. James *et al.*, “Thermodynamic performance of the 3-stage ADR for the Astro-H Soft-X-ray Spectrometer instrument,” *Cryogenics*, vol. 74, pp. 24–30, Mar. 2016. <https://ui.adsabs.harvard.edu/#abs/2016Cryo...74...24S>
- [92] J. Rabb et al, “Ngas scw-4k,” Presentation at the 2013 Space Cryogenics Workshop, 2013.
- [93] D. Durand, R. Colbert, C. Jaco, M. Michaelian, T. Nguyen, M. Petach, and J. Raab, “Mid Infrared Instrument (miri) Cooler Subsystem Prototype Demonstration,” in *Advances in Cryogenic Engineering*, ser. American Institute of Physics Conference Series, J. G. Weisend, J. Barclay, S. Breon *et al.*, Eds., vol. 52, Mar. 2008, pp. 807–814. <https://ui.adsabs.harvard.edu/#abs/2008AIPC..985..807D>
- [94] D. S. Glaister, W. Gully, R. Ross, P. Hendershott, E. Marquardt, and V. Kotsubo, “Ball Aerospace 4-6 K Space Cryocooler,” in *Advances in Cryogenic Engineering: Transactions of the Cryogenic Engineering Conference*, ser. American Institute of Physics Conference Series, I. Weisend, J. G., J. Barclay, S. Breon *et al.*, Eds., vol. 823, Apr. 2006, pp. 632–639. <https://ui.adsabs.harvard.edu/#abs/2006AIPC..823..632G>
- [95] F. Pajot, P. A. R. Ade, J. L. Beney *et al.*, “Planck pre-launch status: HFI ground calibration,” *Astron. Astrophys.*, vol. 520, p. A10, Sep. 2010. <https://ui.adsabs.harvard.edu/#abs/2010A&A...520A..10P>
- [96] C. L. Bennett, M. Bay, M. Halpern *et al.*, “The Microwave Anisotropy Probe Mission,” *Ap. J.*, vol. 583, pp. 1–23, Jan. 2003. <https://ui.adsabs.harvard.edu/#abs/2003ApJ...583....1B>
- [97] J. A. Tauber, N. Mandolini, J. L. Puget *et al.*, “Planck pre-launch status: The Planck mission,” *Astron. Astrophys.*, vol. 520, p. A1, Sep. 2010. <https://ui.adsabs.harvard.edu/#abs/2010A&A...520A..1T>
- [98] Space Exploration Technologies Corp., *Falcon 9 Launch Vehicle: Payload User’s Guide, Rev 2*. Space Exploration Technologies Corp., October 2015. https://www.spacex.com/sites/spacex/files/falcon_9_users_guide_rev_2.0.pdf
- [99] W. Hu, M. M. Hedman, and M. Zaldarriaga, “Benchmark parameters for CMB polarization experiments,” *Phys. Rev. D.*, vol. 67, p. 043004, Feb. 2003. <https://ui.adsabs.harvard.edu/#abs/2003PhRvD..67d3004H>

- [100] H. Kurki-Suonio, E. Keihänen, R. Keskitalo, T. Poutanen, A. S. Sirviö, D. Maino, and C. Burigana, “Destriping CMB temperature and polarization maps,” *Astron. Astrophys.*, vol. 506, pp. 1511–1539, Nov. 2009. <https://ui.adsabs.harvard.edu/#abs/2009A&A...506.1511K>
- [101] Deep Space Network, Jet Propulsion Laboratory, California Institute of Technology, “Deep space network services catalog 820-100, rev. f.” February 2015. <https://deepspace.jpl.nasa.gov/files/820-100-F1.pdf>
- [102] Planck Collaboration, R. Adam, P. A. R. Ade *et al.*, “Planck 2015 results. I. Overview of products and scientific results,” *Astron. Astrophys.*, vol. 594, p. A1, Sep. 2016. <https://ui.adsabs.harvard.edu/#abs/2016A&A...594A...1P>
- [103] D. Dutcher, P. A. R. Ade, Z. Ahmed *et al.*, “Characterization and performance of the second-year SPT-3G focal plane,” in *Society of Photo-Optical Instrumentation Engineers (SPIE) Conference Series*, vol. 10708, Jul. 2018, p. 107081Z. <https://ui.adsabs.harvard.edu/#abs/2018SPIE10708E..1ZD>
- [104] The Simons Observatory Collaboration, P. Ade, J. Aguirre *et al.*, “The Simons Observatory: Science goals and forecasts,” *arXiv e-prints*, Aug. 2018. <https://ui.adsabs.harvard.edu/#abs/2018arXiv180807445T>
- [105] H. Hui, P. A. R. Ade, Z. Ahmed *et al.*, “BICEP Array: a multi-frequency degree-scale CMB polarimeter,” in *Millimeter, Submillimeter, and Far-Infrared Detectors and Instrumentation for Astronomy IX*, ser. Society of Photo-Optical Instrumentation Engineers (SPIE) Conference Series, vol. 10708, Jul. 2018, p. 1070807. <http://adsabs.harvard.edu/abs/2018SPIE10708E..07H>
- [106] B. A. Benson, P. A. R. Ade, Z. Ahmed *et al.*, “SPT-3G: a next-generation cosmic microwave background polarization experiment on the South Pole telescope,” in *Society of Photo-Optical Instrumentation Engineers (SPIE) Conference Series*, ser. Society of Photo-Optical Instrumentation Engineers (SPIE) Conference Series, vol. 9153, Jul. 2014, p. 1. <http://adsabs.harvard.edu/abs/2014SPIE.9153E..1PB>
- [107] Y. Li, J. E. Austermann, J. A. Beall *et al.*, “Performance of the advanced ACTPol low frequency array,” in *Society of Photo-Optical Instrumentation Engineers (SPIE) Conference Series*, vol. 10708, Jul. 2018, p. 107080A. <https://ui.adsabs.harvard.edu/#abs/2018SPIE10708E..0AL>
- [108] BICEP2 and Keck Array Collaborations, P. A. R. Ade, Z. Ahmed *et al.*, “BICEP2 / Keck Array X: Constraints on Primordial Gravitational Waves using Planck, WMAP, and New BICEP2/Keck Observations through the 2015 Season,” *arXiv e-prints*, Oct. 2018. <http://adsabs.harvard.edu/abs/2018arXiv181005216A>
- [109] B. Westbrook, A. Cukierman, A. Lee, A. Suzuki, C. Raum, and W. Holzapfel, “Development of the Next Generation of Multi-chroic Antenna-Coupled Transition Edge Sensor Detectors for CMB Polarimetry,” *Journal of Low Temperature Physics*, vol. 184, pp. 74–81, Jul. 2016. <https://ui.adsabs.harvard.edu/#abs/2016JLTP..184...74W>
- [110] S. M. Simon, J. E. Golec, A. Ali *et al.*, “Feedhorn development and scalability for Simons Observatory and beyond,” in *Society of Photo-Optical Instrumentation Engineers (SPIE) Conference Series*, vol. 10708, Jul. 2018, p. 107084B. <https://ui.adsabs.harvard.edu/#abs/2018SPIE10708E..4BS>
- [111] R. O’Brient, J. Edwards, K. Arnold *et al.*, “Sinuous antennas for cosmic microwave background polarimetry,” in *Society of Photo-Optical Instrumentation Engineers (SPIE) Conference Series*, ser. Presented at the Society of Photo-Optical Instrumentation Engineers (SPIE) Conference, vol. 7020, Aug. 2008. <http://adsabs.harvard.edu/abs/2008SPIE.7020E..37O>
- [112] PICO website, “Study on wobble impact for component separation for the LiteBIRD collaboration.” https://sites.google.com/umn.edu/picomission/home/wobble_errard
- [113] J. G. Staguhn, D. J. Benford, C. A. Allen *et al.*, “GISMO: a 2-millimeter bolometer camera for the IRAM 30 m telescope,” in *Society of Photo-Optical Instrumentation Engineers (SPIE) Conference Series*, vol. 6275, Jun. 2006, p. 62751D. <https://ui.adsabs.harvard.edu/#abs/2006SPIE.6275E..1DS>
- [114] M. Ferlet, G. Laurent, B. Swinyard, J. Glenn, J. Bock, and K. Dohlen, “Characterisation of Herschel-SPIRE flight model optical performances,” in *Space Telescopes and Instrumentation 2008: Optical, Infrared, and Millimeter*, ser. Society of Photo-Optical Instrumentation Engineers (SPIE) Conference Series, vol. 7010, Jul. 2008, p. 70102U. <https://ui.adsabs.harvard.edu/#abs/2008SPIE.7010E..2UF>
- [115] J. T. Sayre, P. Ade, K. A. Aird *et al.*, “Design and characterization of 90 GHz feedhorn-coupled TES polarimeter pixels in the SPTPol camera,” in *Millimeter, Submillimeter, and Far-Infrared Detectors and Instrumentation for Astronomy VI*, vol. 8452, Sep. 2012, p. 845239. <https://ui.adsabs.harvard.edu/#abs/2012SPIE.8452E..39S>
- [116] R. Gualtieri, J. P. Filippini, P. A. R. Ade *et al.*, “SPIDER: CMB Polarimetry from the Edge of Space,” *Journal of Low Temperature Physics*, vol. 193, pp. 1112–1121, Dec. 2018. <http://adsabs.harvard.edu/abs/2018JLTP..193..1112G>

//adsabs.harvard.edu/abs/2018JLTP..193.1112G

- [117] J. P. Filippini et al, in preparation, 2019.
- [118] W. S. Holland, D. Bintley, E. L. Chapin *et al.*, “SCUBA-2: the 10 000 pixel bolometer camera on the James Clerk Maxwell Telescope,” *MNRAS*, vol. 430, pp. 2513–2533, Apr. 2013. <https://ui.adsabs.harvard.edu/#abs/2013MNRAS.430.2513H>
- [119] W. B. Doriese, K. M. Morgan, D. A. Bennett *et al.*, “Developments in Time-Division Multiplexing of X-ray Transition-Edge Sensors,” *Journal of Low Temperature Physics*, vol. 184, pp. 389–395, Jul. 2016. <https://ui.adsabs.harvard.edu/#abs/2016JLTP..184..389D>
- [120] B. Dober, D. T. Becker, D. A. Bennett *et al.*, “Microwave SQUID multiplexer demonstration for cosmic microwave background imagers,” *Applied Physics Letters*, vol. 111, p. 243510, Dec. 2017. <https://ui.adsabs.harvard.edu/#abs/2017ApPhL.111x3510D>
- [121] K. D. Irwin and K. W. Lehnert, “Microwave SQUID multiplexer,” *Applied Physics Letters*, vol. 85, p. 2107, Sep. 2004. <https://ui.adsabs.harvard.edu/#abs/2004ApPhL..85.2107I>
- [122] H. McCarrick, G. Jones, B. R. Johnson *et al.*, “Design and performance of dual-polarization lumped-element kinetic inductance detectors for millimeter-wave polarimetry,” *Astron. Astrophys.*, vol. 610, p. A45, Feb. 2018. <http://adsabs.harvard.edu/abs/2018A%26A...610A..45M>
- [123] B. A. Steinbach, J. J. Bock, H. T. Nguyen, R. C. O’Brient, and A. D. Turner, “Thermal Kinetic Inductance Detectors for Ground-Based Millimeter-Wave Cosmology,” *Journal of Low Temperature Physics*, vol. 193, pp. 88–95, Nov. 2018. <https://ui.adsabs.harvard.edu/#abs/2018JLTP..193..88S>
- [124] B. R. Johnson, D. Flanigan, M. H. Abitbol *et al.*, “Development of Multi-chroic MKIDs for Next-Generation CMB Polarization Studies,” *Journal of Low Temperature Physics*, vol. 193, pp. 103–112, Nov. 2018. <http://adsabs.harvard.edu/abs/2018JLTP..193..103J>
- [125] PICO website, “PICO: Probe of Inflation and Cosmic Origins.” <https://sites.google.com/umn.edu/picomission>
- [126] J. Mrozinski and M. DiNicola, “NICM: Cryocooler,” NASA 2017 Cost Symposium Presentations, August 2017. https://www.nasa.gov/offices/ocfo/cost_symposium/2017_presentations
- [127] P. Gloesener, “Large Aluminium Convex Mirror for the Cryo-Optical Test of the Planck Primary Reflector,” in *ESA Special Publication*, vol. 621, Jun. 2006, p. 43. <https://ui.adsabs.harvard.edu/#abs/2006ESASP.621E..43G>
- [128] Y. Toulemon, T. Passvogel, G. Pillbrat, D. de Chambure, D. Pierot, and D. Castel, “The 3.5m all SiC telescope for Herschel,” in *5th International Conference on Space Optics*, B. Warmbein, Ed., vol. 554, Jun. 2004, pp. 341–348. <https://ui.adsabs.harvard.edu/#abs/2004ESASP.554..341T>
- [129] S. Bard, “Development of a High-Performance Cryogenic Radiator with V-Groove Radiation Shields,” *Journal of Spacecraft and Rockets*, vol. 24, pp. 193–197, May 1987. <https://ui.adsabs.harvard.edu/#abs/1987JSpRo..24..193B>